

SEARCH FOR BLUE COMPACT DWARF GALAXIES DURING QUIESCENCE II: METALLICITIES OF GAS AND STARS, AGES, AND STAR-FORMATION RATES

J. SÁNCHEZ ALMEIDA¹ J. A. L. AGUERRI¹,
C. MUÑOZ-TUÑÓN¹, A. VAZDEKIS¹

Draft version October 31, 2018

ABSTRACT

We examine the metallicity and age of a large set of SDSS/DR6 galaxies that may be Blue Compact Dwarf (BCD) galaxies during quiescence (QBCDs). The individual spectra are first classified and then averaged to reduce noise. The metallicity inferred from emission lines (tracing ionized gas) exceeds by ~ 0.35 dex the metallicity inferred from absorption lines (tracing stars). Such a small difference is significant according to our error budget estimate. The same procedure was applied to a reference sample of BCDs, and in this case the two metallicities agree, being also consistent with the stellar metallicity in QBCDs. Chemical evolution models indicate that the gas metallicity of QBCDs is too high to be representative of the galaxy as a whole, but it can represent a small fraction of the galactic gas, self enriched by previous starbursts. The luminosity weighted stellar age of QBCDs spans the whole range between 1 and 10 Gyr, whereas it is always smaller than 1 Gyr for BCDs. Our stellar ages and metallicities rely on a single stellar population spectrum fitting procedure, which we have specifically developed for this work using the stellar library MILES.

Subject headings: Galaxies: abundances – Galaxies: dwarf – Galaxies: evolution – Galaxies: ISM – Galaxies: starburst

1. INTRODUCTION

In the hierarchical picture of galaxy formation, large galaxies arise through the assembly of smaller aggregates (e.g., White & Frenk 1991; Diemand et al. 2007), and metal-deficient dwarf galaxies are possibly the closest examples we can find of the elementary primordial units from which galaxies assembled. In the downsizing paradigm, large galaxies form metals early on (e.g., Cowie et al. 1996; Kauffmann et al. 2003), and only low metallicity dwarfs may still keep a fossil record of the pristine Inter-Stellar Medium (ISM). For one reason or another, Blue Compact Dwarf (BCD) galaxies seem to probe early phases of the Universe. They combine the two required ingredients, i.e., they are dwarfs having record-breaking low metallicities (e.g. Kunth & Östlin 2000; Izotov et al. 2005). BCD galaxies have been used to constrain, e.g., the properties of the first (Pop III) stars that polluted the primordial ISM at the time of galaxy formation (e.g., Bromm & Larson 2004), or the primordial He abundance inherited from big-bang nucleosynthesis (e.g., Izotov et al. 2007).

BCD galaxies have been extensively studied during the last 35 years (e.g. Sargent & Searle 1970; Searle & Sargent 1972; Silk et al. 1987; Davies & Phillipps 1988; Papaderos et al. 1996a; Telles & Terlevich 1997; Cairós et al. 2001; Gil de Paz et al. 2003; Gil de Paz & Madore 2005; Amorín et al. 2007). However, the way they grow up and evolve remains unknown. The intense starburst that characterizes BCDs lasts only a few Myr (e.g., Mas-Hesse & Kunth 1999; Thuan 1991). BCDs seem to be undergoing a transient but we ignore how they reach such state, and what happens to them afterwards.

Consequently, identifying precursors and descendants of BCDs would be a major breakthrough in deciphering the nature and the functioning of these special galaxies. It will facilitate using them as reliable tools in cosmological studies.

Evolutionary connections between different dwarf galaxies and BCDs have been both proposed and questioned in the literature (e.g., Searle & Sargent 1972; Silk et al. 1987; Davies & Phillipps 1988; Papaderos et al. 1996a; Telles & Terlevich 1997; Gil de Paz & Madore 2005; Dellenbusch et al. 2007; Amorín et al. 2009). In an attempt to complement these efforts, we carried out a search for galaxies that may be BCD during the periods where the major starburst is gone, i.e., quiescent BCDs or, for short, QBCDs (Sánchez Almeida et al. 2008, hereafter Paper I). We addressed the issue from a new perspective. Most BCDs show a red low surface brightness component which should exist before the present starburst sets in and should remain once the starburst fades away (Loose & Thuan 1986; Papaderos et al. 1996b). By carefully removing the starburst, this underlying component has been studied and characterized in the literature (e.g., Noeske et al. 2003; Caon et al. 2005; Amorín et al. 2007, 2009). We searched the SDSS/DR6 database for isolated galaxies with the luminosity, color, surface brightness, and concentration characteristic of the low surface brightness component underlying the BCDs (Paper I). Assuming that the underlying low surface brightness galaxy remains unaltered after each starburst exhaustion, the targets thus selected could be QBCDs. The search yielded some 21500 QBCD candidates, with properties pointing out that they may be indeed pre or post BCDs. In particular, they have the same luminosity function as the BCDs, although they are thirty times more numerous. The results suggested an evolutive sequence where BCDs undergo many short starburst

Electronic address: jos@iac.es, jalfonso@iac.es, cmt@iac.es, vazdekis@iac.es
¹Instituto de Astrofísica de Canarias, E-38205 La Laguna, Tenerife, Spain

phases during their lifetimes, as proposed long ago by Searle & Sargent (1972). In between bursts, the galaxies show up as QBCDs in a low activity state of various degrees lasting thirty times longer than the bursts. Statistically, QBCDs should undergo a BCD phase every 300 Myr and lasting some 10 Myr. This sequence of BCD and QBCD phases can be maintained during several Hubble times, and the most active QBCDs are indeed BCDs. Paper I carries out the differential comparison with BCDs by selecting the sample of BCDs also from SDSS/DR6, and employing the same procedures used to retrieve the QBCDs.

In spite of all these agreeable features, the evolutive link between BCDs and QBCDs presents an important difficulty posed in Paper I. The QBCD oxygen abundance was estimated to be 0.35 dex systematically larger than the oxygen abundance of the BCDs. This makes the role of QBCDs as BCD precursors questionable since starbursts increase metallicity, and the putative precursors (QBCDs) should have lower metallicity than their descendants (BCDs). Paper I offered a few alternatives to clear out the difficulty, most of which were related with the infall of metal poor gas before the starburst sets in. In addition, we speculated that the metallicity assigned to the QBCDs may be biased, with the *true* QBCD metallicities much lower than the observed ones, and close to the observed BCD metallicities. We derive the oxygen abundance from emission lines produced in H II regions, which trace the ISM in those places now going through a star-formation episode. In the case of QBCDs, the star formation rate is quite small ($< 0.1 M_{\odot} \text{y}^{-1}$ even for the brightest ones; § 8), therefore the volume of galactic gas sampled by the measurement is very small too. The question arises as to whether the abundance of this gas is representative of the total galactic gas. If it is not, then it could explain a false overabundance of oxygen in our QBCD candidates. The sampled gas may not be properly mixed up with the galactic ISM and, therefore, be self metal enriched by successive starbursts.

The possibility that the metallicity deduced from emission lines may be contaminated by recent starbursts has been previously mentioned in the literature (e.g., Kunth & Sargent 1986; Thuan et al. 2004; Dalcanton 2007). The mixing of the ISM is a slow process, which leaves behind a patchy medium (e.g., Tenorio-Tagle 1996; de Avillez & Mac Low 2002).

The present work was originally meant at testing the main conjecture in Paper I, namely, that the emission line derived metallicity overestimates the *true* average metallicity of the QBCD gas. If so, it should be significantly larger than the metallicity of other galactic components, in particular, the metallicity of the stars. This seems to be the case (§ 6), but in the way of working it out, several other properties of QBCDs (and BCDs) have emerged. These results are described here in fairly broad terms, keeping in mind their potential interest outside the specific original motivation of the work. In particular, QBCD galaxies are quite common (one out of each three local dwarfs; Paper I), so that their properties may also be representative of the whole class of dwarf galaxies.

The paper is organized as follows: § 2 summarizes the main observational properties of the Sloan Digital Sky Survey/Data Release 6 (SDSS/DR6) spectra used in our

analysis. § 3 explains the classification of spectra before averaging them out to improve the signal-to-noise ratio. By fitting the observed QBCD spectra with synthetic spectra, we assign ages and metallicities to the stellar component of the galaxies (§ 4). Gas metallicities are estimated in § 5, with their uncertainties critically assessed in App. A. § 6 puts forward the excess of gas metallicity with respect to the metallicity of the stellar component. Ages and stellar content are analyzed in § 7. Chemical evolution model galaxies able to account for the differences between stellar and nebular metallicities are discussed in § 8, where we also have to estimate Star Formation Rates (SFRs). Finally, the main results and their implications are discussed in § 9.

2. DATA SET: SDSS SPECTRA

We aim at assigning metallicities to the stellar component of the QBCD candidates selected in Paper I. The original galaxies were chosen within the SDSS spectroscopic catalog, to have redshifts from which we derive absolute magnitudes (mean redshift 0.030, with a standard deviation of 0.014). The present analysis of stellar metallicities is based on these SDSS spectra. For the sake of comprehensiveness, their main characteristics are summarized here. A more detailed account can be found in Stoughton et al. (2002), Adelman-McCarthy et al. (2008), and also in the SDSS website (<http://www.sdss.org/dr6>).

The SDSS spectrograph has two independent arms, with a dichroic separating the blue beam and the red beam at 6150 Å. It simultaneously renders a spectral range from 3800 Å to 9200 Å, with a spectral resolution between 1800 and 2200. The sampling is linear in logarithmic wavelength, with a mean dispersion of 1.1 \AA pix^{-1} in the blue and 1.8 \AA pix^{-1} in the red. Repeated 15 min exposure spectra are integrated to yield a S/N per pixel > 4 when the apparent magnitude in the *g* bandpass is 20.2. The spectrograph is fed by fibers which subtend about $3''$ on the sky. Most galaxies are larger than this size, therefore, the spectra sample only their central parts (e.g., 89% of the QBCD galaxies have an effective radius larger than half the fiber diameter). We retrieve the 21493 QBCD spectra and the 1609 BCD spectra in FITS format from the SDSS Data Archive Server. All spectra were re-sampled to a common rest-frame wavelength scale that matches the spectral library used in § 4 (Sánchez-Blázquez et al. 2006; Cenarro et al. 2007). We use linear interpolation to oversample the original spectra with a constant dispersion of 0.9 \AA pix^{-1} . The spectra were normalized to the flux in the *g* color filter (effective wavelength $\simeq 4825 \text{ \AA}$), a normalization factor that we compute from each spectra using the transmission curve downloaded from the SDSS website.

3. CLASSIFICATION OF GALAXY SPECTRA

As we will discuss later on (§ 4.2), the S/N of the individual SDSS spectra is insufficient to estimate the metallicity of the stellar component. We improve the S/N ratio to acceptable levels by averaging similar spectra (a technique often referred to as *stacking*; see, e.g. Ellison et al. 2000). Before averaging, the spectra have been classified in alike sets using a cluster analysis algorithm. We employ the simple *k-means clustering* (see, e.g., Everitt

1995, Chapter 5). A number k of template spectra are selected at random from the full set. Each template spectrum is assumed to be a cluster center, and each spectrum of the data set is assigned to the closest cluster center (closest in a least squares sense). Once all spectra in the dataset have been classified, the cluster center is re-computed as the average of all spectra in the cluster. This procedure is iterated with the new cluster centers, and it quits when no spectrum is re-classified in two consecutive steps. The algorithm is simple and fast, but it yields different clusters with each random initialization – the final cluster centers keep some memory of the original randomly chosen cluster centers. This drawback does not interfere with our purpose of selecting sub-sets of similar spectra suitable for averaging because, independently of the initialization, the clusters always contain similar spectra. The algorithm forces all spectra in a class to be similar to the cluster center, and therefore, similar among them. The number of clusters k is arbitrarily chosen but, in practice, the results are insensitive to such selection since only a few clusters possess a significant number of members, so that the rest are discarded. Figure 1 shows the number of elements in each class of QBCD spectra resulting from applying the procedure. The classes have been sorted and labelled according to the number of elements, with Class 0 the most numerous, Class 1 the second most numerous, and so on (percentages are given in Table 1). Figure 2 shows the average spectrum corresponding to the first nine most numerous classes. The classification was carried out using four spectral bandpasses containing emission lines (the bandpasses are indicated as dotted lines in Fig 2, Class 0, and also in Fig. 3). The use of these particular bandpasses emphasizes the contribution of the emission lines for classification which, otherwise, would be completely overridden by the continuum. We select bandpasses throughout the full spectral range to assure that the global trend of the continuum is considered when classifying. There seems to be continuous variation of properties which, in the end, give rise to a large variety of shapes. From spectra without significant emission lines (Class 3), to spectra with red continuum and emission lines (Class 7), to blue continua with moderate emission lines (Class 4). The most numerous Class 0 has blue continuum and presents emission lines.

The scatter among the spectra belonging to a class depends on wavelength, and it is largest in the intense emission lines. As it is illustrated in Fig. 3 with Class 0 spectrum, it is of the order of 10% in the spectral ranges with absorption lines, and it can be of the order of 50% in the regions having strong emission lines (see the dashed line in Fig. 3, which corresponds to the *rms* fluctuations among all the spectra in the class divided by the mean spectrum).

The same classification procedure was also applied to the control set of BCDs. Representative spectra of the most numerous classes are shown in Fig. 4, also sorted and labelled according to the number of galaxies in the class. The most conspicuous differences with respect to QBCD spectra are the strength of the emission lines, and the (barely visible but always present) blue continua. The fraction of galaxies in each class is listed in Table 1.

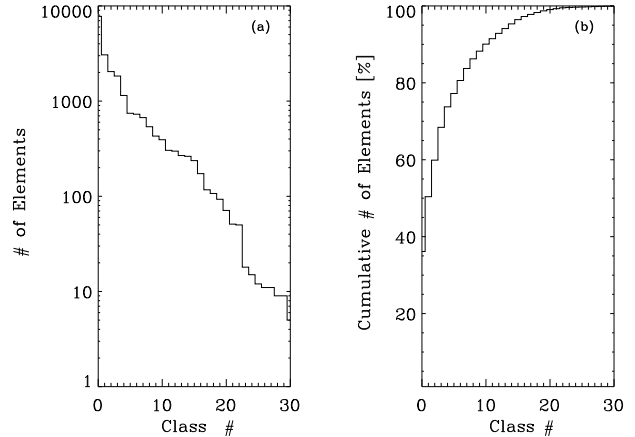


FIG. 1.— (a) Histogram with the number of QBCD galaxies corresponding to each class. (b) Normalized cumulative histogram, i.e., fraction of QBCD galaxies from Class 0 to the each class #. It is given in percent. Note that the first ten classes include 90 % of the QBCDs.

3.1. Green valley QBCDs

One of the findings of the SDSS is the existence of a galaxy color sequence with well defined bi-modality (e.g., Balogh et al. 2004). Paper I shows how QBCDs occupy all the color sequence between the blue and the red clumps. It turns out that the classification has been able to separate galaxies in the red sequence, galaxies in the blue sequence, as well as those in between (often referred to as *green valley* galaxies, e.g., Salim et al. 2007). Figure 5 shows color vs color scatter plots for the QBCDs, the BCDs, as well as the most usual QBCD classes separately. It also includes the somewhat arbitrary boundary between the red and the blue sequences worked out in Paper I (the dashed line). The classification does a fair job in splitting the galaxies in colors. Among the most numerous classes, it turns out that only Class 3 belong to the red sequence. (Class 3 has no emission lines; see Fig. 2.) In addition, we noticed that Class 1 seems to include all the *green valley* galaxies, i.e., the transition galaxies, central to understand how and why galaxies move back and forth in the color sequence (e.g., Springel et al. 2005; Cattaneo et al. 2006). The goodness of this green valley galaxy selection method can be appreciated by comparing the top left plot with the bottom right plot in Fig. 5. The two of them include the same QBCD galaxies except for Class 1. A clear gap splits up the red and the blue clumps.

Since different classes have different colors, and the QBCD present a clear color-(nebular)metallicity relationship (Paper I), different classes have different metallicities too. Scatter plots of metallicity vs absolute magnitude are shown in Fig. 6. Here and throughout we use the recipe in Pettini & Pagel (2004) to compute nebular metallicities from the N2 strong-line ratio (see also § 5). It upgrades of the classical calibration by Denicoló et al. (2002) used in Paper I (Shi et al. 2005, and references therein). Late types (e.g., Class 0) are metal poor as compared to the transition objects included in Class 1. These green valley galaxies have solar metallicity. The few galaxies in the red clump with emission lines (Class 7; see Fig. 2) seems to have slightly super-solar metallic-

TABLE 1
PROPERTIES OF QBCD CLASSES AND BCD CLASSES.

Galaxy Type	Class	Fraction ^a [%]	Stellar Metallicity ^b	Stellar Age ^c [Gyr]	Nebular Metallicity ^d	H α EW ^e [Å]	[NII] EW ^f [Å]
QBCD	0	36.1	-0.44±0.03	1.7±0.2	-0.12±0.18	22.3	5.2
	1	14.3	-0.39±0.02	5.2±1.4	0.05±0.18	5.3	2.5
	2	9.5	-0.32±0.12	1.1±0.6	-0.25±0.18	50.4	6.9
	3	8.5	-0.33±0.02	11.1±1.7
	4	5.3	-0.36±0.08	1.0±0.1	-0.26±0.18	14.5	1.9
	5	3.5	-0.68±0.28	1.1±3.0	-0.40±0.18	99.9	7.5
	6	3.4	-0.44±0.11	1.1±0.2	-0.25±0.18	31.6	4.4
	7	3.1	-0.42±0.04	4.1±1.2	0.05±0.18	8.4	3.9
	8	2.5	-0.37±0.07	2.7±1.7	-0.01±0.18	27.6	10.0
BCD	9	2.0	-0.30±0.02	17.8±0.4
	0	46.9	-0.33±0.08	0.9±0.1	-0.38±0.18	81.2	6.7
	1	12.7	-0.34±0.22	1.0±0.8	-0.41±0.18	160.2	11.7
	2	7.9	-0.37±0.40	0.9±2.5	-0.49±0.18	241.6	12.4
	3	7.4	-0.39±0.17	1.1±0.8	-0.37±0.18	125.9	10.7
	4	6.5	-0.41±0.21	0.9±0.6	-0.51±0.18	142.0	6.5
	5	3.8	-0.34±0.15	1.0±0.4	-0.35±0.18	93.7	8.8
6	3.5	-0.34±0.54	1.1±4.6	-0.48±0.18	333.0	17.1	

NOTE. — It includes those classes containing 90% of the galaxies.

^a Percentage of galaxies represented by the class.

^b In logarithm scale, referred to the solar metallicity. Errors from Monte Carlo analysis in § 4.

^c Errors from the Monte Carlo analysis in § 4.

^d In logarithm scale, referred to the solar metallicity. Its error has been taken from Pettini & Pagel (2004).

^e Equivalent width of H α . No data implies line in absorption.

^f Equivalent width of [NII] λ 6583. No data implies line in absorption.

ity (Fig. 6).

The k-mean clustering classification provides an automatic method to identify spectra of green valley galaxies. It works for QBCDs, however, there is no clear reason why it should be restricted to them. It may be valid for any type of galaxy, even outside the particular set of dwarfs we are dealing with. We elaborate on this possibility in § 9.

4. DETERMINATION OF STELLAR METALLICITIES AND AGES

The stellar content of a galaxy can be studied through modeling and interpretation of the absorption features in the integrated spectrum. The analysis of line-strength indices, mainly those of the Lick system (Worthey et al. 1994; Worthey & Ottaviani 1997), has been the most common approach for studying the stellar metallicities and ages. Most studies have been focused on early-type galaxies, with stellar populations typically older than 1 Gyr (e.g., Trager et al. 1998, and references therein). The use of age-sensitive Balmer line indices, e.g., H β , and metallicity-sensitive indices, e.g., Mgb, allows us to lift in part the age-metallicity degeneracy affecting the stellar populations of early-type galaxies (e.g., Worthey et al. 1994; Vazdekis & Arimoto 1999). However, these line strengths, and particularly the Balmer indices, are not optimal for analyzing our galaxy spectra, since they are filled-in with nebular emission (Fig. 2). Here we take a different approach, and ages and metallicities are estimated by direct comparison of the observed spectra with model spectra from stellar population syntheses. The full

spectral range is used simultaneously. This alternative strategy has a respectable tradition (see Koleva et al. 2008, and references therein), and it allows us to easily overcome the problem of emission lines by masking them out. Emission lines represent only a small fraction of the spectral range, and the rest of the spectrum can be used to extract the required information (see below). We use an updated version of the models by Vazdekis (1999), which provide spectral energy distributions of single-age, single-metallicity stellar populations (SSPs) on the basis of the stellar spectral library MILES (Sánchez-Blázquez et al. 2006; Cenarro et al. 2007). The MILES SSP spectra combine, according to a Salpeter initial mass function distribution, a suite of stellar spectra from 0.09 M_{\odot} to 100 M_{\odot} . They have a resolution of $\simeq 2.3$ Å, a spectral range from 3540 Å to 7410 Å, and a dispersion of 0.9 Å pix⁻¹. MILES SSP extends the range of ages of Vazdekis (1999), and now it covers from 0.1 Gyr to 17.8 Gyr. MILES SSP spectra span a range of metallicities² between -1.7 and +0.2. The grid includes 276 SSP spectra, with 46 samples equispaced in logarithmic time, and 6 steps in metallicity. The range of metallicities and ages fits in well the values to be expected for QBCD (see § 1). As far as the wavelength sampling and wavelength coverage are concerned, MILES SSP spectral resolution is comparable to SDSS (although better), but it misses the reddest 1800 Å of the SDSS spectral range. The uncovered 20% of the SDSS spectral range

² In the usual logarithmic scale referred to the solar metallicity Z_{\odot} , i.e., $\log(Z_s/Z_{\odot})$ with Z_s the fraction of mass in metals.

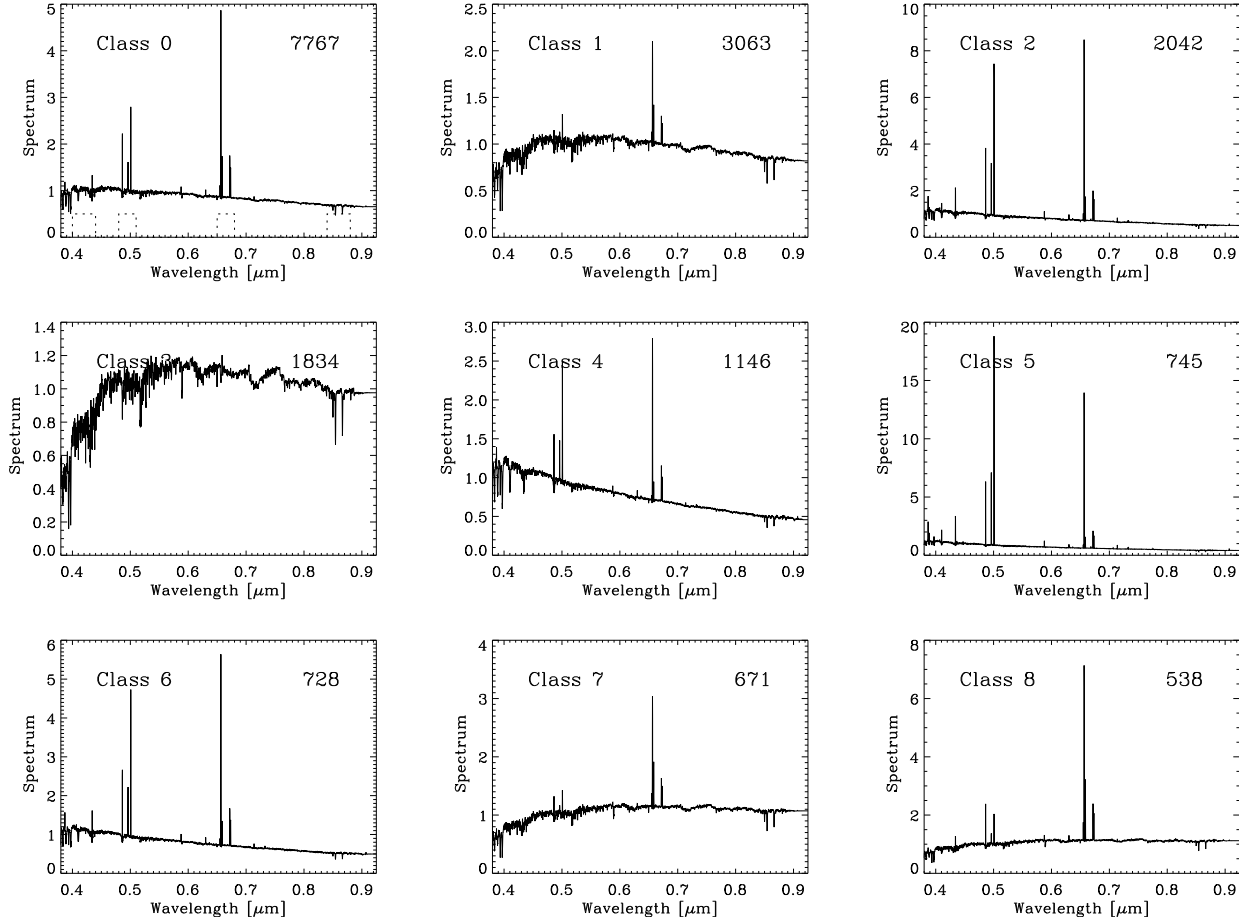


FIG. 2.— Average spectra of the first nine most abundant QBCD classes. Together with the class identifier, the insets of the figures give the number of galaxies in the class. Wavelengths are in μm , and the range of ordinates is different for the different plots. All spectra are normalized to the flux in the g filter. The dotted line shown together with Class 0 indicates the band-passes used to classify spectra (i.e., those wavelengths where it is zero were disregarded for classification).

is in the near IR, where the number of spectral lines decreases significantly. Keeping in mind all these variables, MILES SSP meets very well our needs.

The fits are carried out by direct comparison of each average profile representative of a class with all spectra in the MILES SSP library, smeared to three spectral resolutions (the original one, the original one plus 2.5 \AA , and the original one plus 3.5 \AA). Considering various broadenings is required to account for stellar motions, as well as for the difference of spectral resolution between MILES SSP and SDSS. The observed spectrum is compared with each synthetic spectrum, and closest one in a least-squares sense is chosen as best fit. The comparison was carried out with a few constraints which try to minimize potential biases. (1) A 100 \AA running-box mean of the original spectra was removed from observed and synthetic spectra. By removing the continua, the results of the fits are not very sensitive to the extinction, a miscalibration of the spectra, the uncorrected differential refraction (Izotov et al. 2006), and so on, which affect the continua but not so much the relative intensity of adjacent spectral lines. Moreover, it guarantees that ages and metallicities are inferred from spectral lines, with negligible contribution from the global shape of the

continuum. (2) We assume the observed spectra O_i to be a linear combination of a starburst spectrum N_i plus an stellar spectrum S_i ,

$$O_i = \alpha N_i + \beta S_i, \quad (1)$$

with the subscript i representing the i -th wavelength, and α and β being two scaling constants. The starburst spectrum has strong emission lines and little continuum, therefore, one could simply neglect the core of the emission lines when carrying out the fits (i.e., one could mask out the emission lines and set $N_i = 0$ in equation [1]). Here we go a step further so that the (small) contamination by N_i outside emission lines is estimated and subtracted out. The decontamination procedure works as follows. At the emission line cores of O_i , the spectrum is dominated by N_i so that,

$$O_i (1 - w_i) = (1 - w_i)(\alpha N_i + \beta S_i) \simeq (1 - w_i) \alpha N_i, \quad (2)$$

with w_i a properly chosen weight which is zero in the emission cores and one elsewhere, i.e.,

$$w_i = \begin{cases} 0 & \text{emission lines,} \\ 1 & \text{elsewhere.} \end{cases} \quad (3)$$

Using the different classes of BCD spectra as proxies for N_i , we choose for each O_i the N_i BCD spectrum that

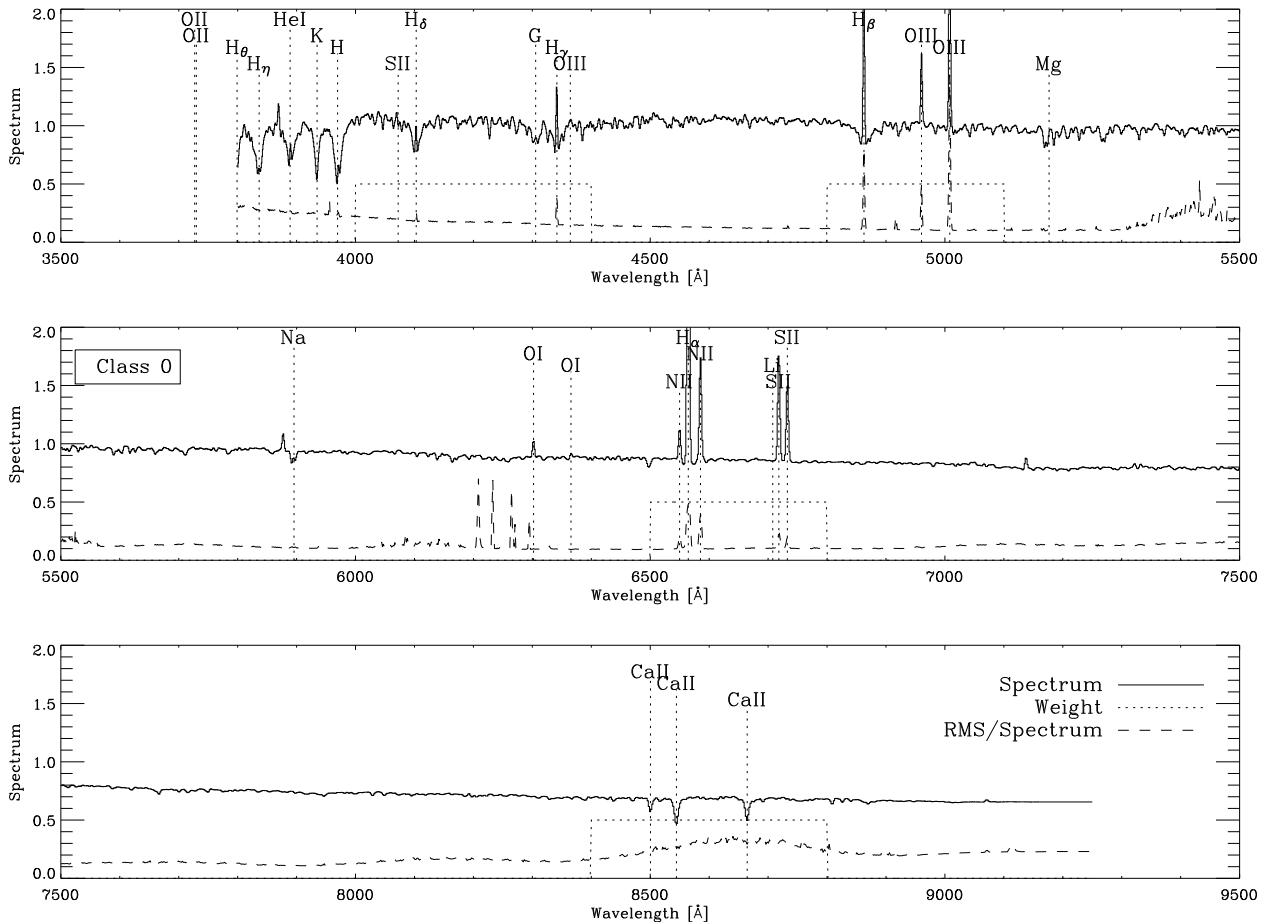


FIG. 3.— Expanded version of the spectrum of Class 0 in Fig. 2. In addition to the spectrum itself (the solid line), the plot includes the *rms* fluctuations among all the spectra in the class divided by the mean spectrum (the dashed line). The bandpasses used for classification are shown as dotted line. The plot also labels several typical spectral features. Wavelengths are given in Å. The large fluctuations between 6200Å and 6300Å are produced by telluric lines (e.g., § 4.2 in Graves et al. 2009). Their presence does not affect our fits (see the residuals at these wavelengths in Figs. 7 and 8).

minimizes the appropriate merit function,

$$\chi^2 = \sum_i [(O_i - \alpha N_i)^2 (1 - w_i)^2], \quad (4)$$

with

$$\alpha = \left[\sum_i O_i N_i (1 - w_i)^2 \right] / \left[\sum_j N_j^2 (1 - w_j)^2 \right], \quad (5)$$

the latter being just a least squares estimate of the scaling factor that best fit the emission lines of O_i once N_i is given. Note that the weight $(1 - w_i)$ in equation (4) assures that only the emission lines contribute to χ^2 . The N_i and α thus derived allows us to compute the observed spectrum corrected for emission, O_i^* ,

$$O_i^* = O_i - \alpha N_i = \beta S_i. \quad (6)$$

The best fitting MILES SSP spectrum is obtained by repeating the same procedure with O_i^* but masking out the emission lines, i.e., defining the merit function for each MILES SSP spectrum $S_i(t, Z_s)$ as,

$$\chi^2(t, Z_s) = \sum_i [(O_i^* - \beta S_i(t, Z_s))^2 w_i^2], \quad (7)$$

where

$$\beta = \left[\sum_i O_i^* S_i(t, Z_s) w_i^2 \right] / \left[\sum_j S_j(t, Z_s)^2 w_j^2 \right]. \quad (8)$$

The expressions explicitly include the dependence of the synthetic spectrum on the age of the starburst, t , and the stellar metallicity, Z_s , i.e., $S_i(t, Z_s)$. The weight w_i in equation (7) cancels out the contribution of the emission lines, rendering the correction (6) of secondary importance. The weights w_i are assigned so as to cover the emission line cores observed in BCD spectra. Examples of these weights are the (thin) solid lines in Figs. 7 and 8. The positions of the minima of these broken lines mark the wavelengths discarded from the fits. The fitting procedure described above was also applied to BCD spectra. In this case we cannot correct for the starburst since BCDs are used as template starburst spectra. We just mask out the emission lines and force $\alpha = 0$ in equation (6).

As judged from visual inspection, the best fitting model spectrum reproduces very well the observed spectra; see, e.g., Fig. 7. Error bars cannot be assigned using traditional methods based on the Hessian matrix of χ^2 , since we do not have a continuous function $\chi^2(t, Z_s)$

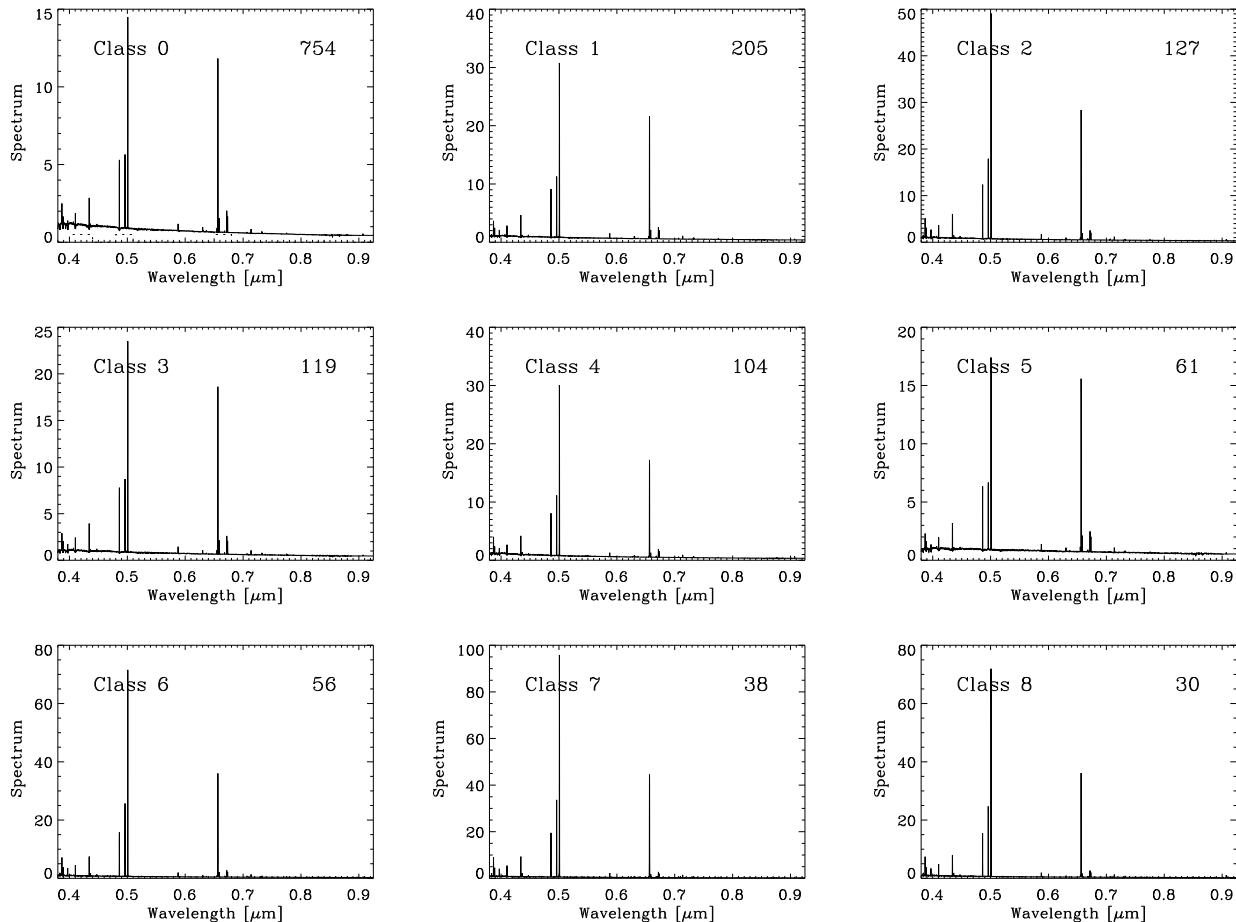


FIG. 4.— Same as Fig. 2 but for BCD galaxies.

to compute the partial derivatives with respect to age and metallicity. We resort to Monte Carlo simulations to assign confidence intervals. Gaussian noise with the standard deviation of the residuals is added to the best fitting model spectrum. This mock observation is analyzed as the real observation to get an age and a metallicity which, in general, differ from those of the best fitting model spectrum. The procedure is repeated 1000 times, which provides a range of ages and metallicities consistent with the best fitting model spectrum and the residual of the fit. Confidence intervals thus assigned reveal a serious problem of degeneracy in the metallicity estimate. The standard deviation of the most common QBCD Class 0 turns out to be 0.25 dex, which allows for any metallicity between -0.20 and -0.70 . Such degeneracy in metallicity is the young stellar population equivalent of the well known age-metallicity degeneracy appearing in early-type galaxy dating (e.g., Worthey 1994). We managed to sort out the degeneracy problem by overweighting the contribution of those spectral bandpasses that are known to be particularly sensitive to metallicity. Specifically, the merit function in the definition (7) is now,

$$w_i = \begin{cases} 0 & \text{emission lines,} \\ W & \text{metallicity sensitive bandpasses,} \\ 1 & \text{elsewhere,} \end{cases} \quad (9)$$

with $W > 1$ for overweighting. The band passes were selected from the Lick index system (Worthey et al. 1994), which was specifically designed for estimating ages and metallicities in the integrated light of stellar populations. In order to find out which are the Lick indexes most sensitive to metallicity in our domain of ages, we computed the variation of the indexes with metallicity at a given age. Some results for the MILES SSP library are shown in Fig. 9. Among the 21 indexes defined by Worthey et al. (1994), we select the three indexes in the top row because they show the largest variation with metallicity. Figure 9, bottom row, also includes three other indexes commonly used in metallicity studies of early-type galaxies (e.g., they are combined to form the so-called [MgFe] index; see González 1993; Thomas et al. 2003). The range of variation is clearly inferior to the variation of the indexes that we select. The bandpasses of the three selected indexes, Fe4383, Fe4531, and Fe4668, are indicated in Figs 7a and 8a as the wavelengths where the thin solid line representing the weight w_i goes out of scale. We tried with various overweights ($W = 10, 20, 50$ and 100), to finally choose $W = 50$ since the trial fits indicate that the inferred metallicity does not depend on the actual weight when the weights are large enough. The use of these overweights improves the metallicity estimate to a large extent. We repeated the Monte Carlo simulation described above, and the random errors of

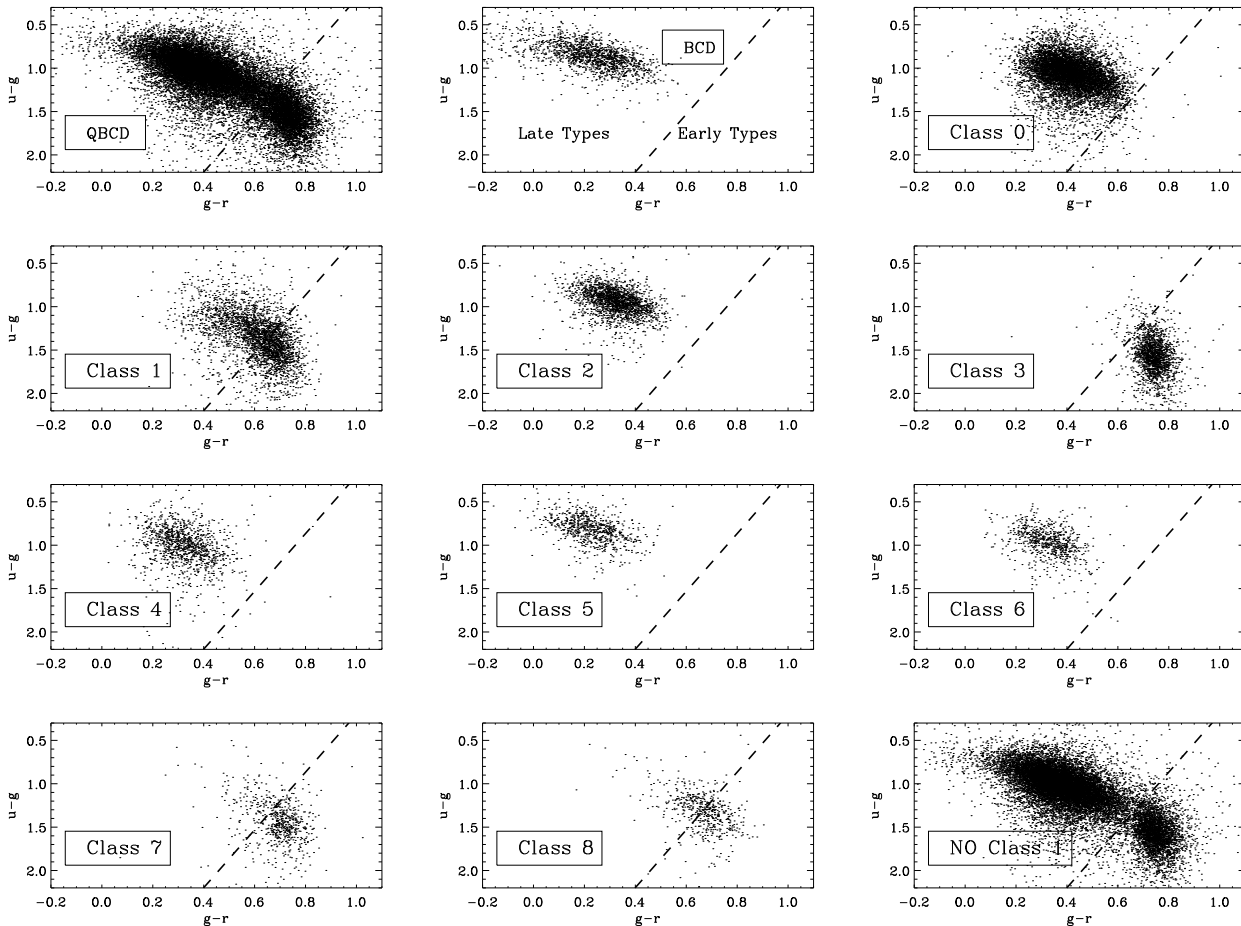


FIG. 5.— Color vs color scatter plots for the QBCDs, the BCDs, and the most usual QBCD classes separately. The insets specify each galaxy group. The dashed line is the same in all plots, and it was worked out in Paper I to separate the blue and the red sequences. Note that most QBCDs belong to the blue sequence. Almost all galaxies in the red clump correspond to Class 3. Moreover, Class 1 seems to gather most galaxies in the so-called *green valley* between the red and the blue sequences (c.f. the plots in top left and the bottom right corners, which are identical except that Class 1 has been removed from the latter).

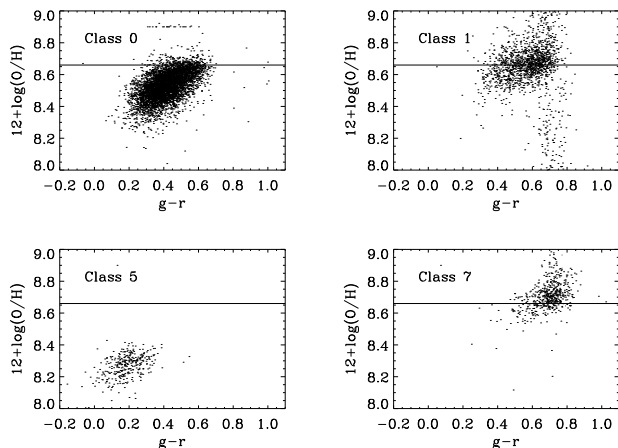


FIG. 6.— Scatter plot of oxygen abundance vs $g-r$ color for some representative QBCD classes. The horizontal solid line corresponds to the solar metallicity as given by Grevesse et al. (2007). Class 3 is not included because it lacks of the emission lines needed to compute nebular abundances.

QBCD Class 0 decrease by almost an order of magnitude with respect to the case where W was set to one.

Table 1 includes the standard deviation for the ages and metallicities of all major QBCD and BCD classes. They will be employed as 1σ errors in the discussions along the paper. The small value of these random errors has been independently corroborated by a bootstrap error estimate (e.g., Moore et al. 2003). A caveat is in order, though. These small errors only indicate that the best fitting MILES SSP spectrum is well defined, i.e., among the MILES SSP set, a few spectra reproduce the observation clearly better than the rest. Our procedure does not account for systematic errors, which may dominate the error budget (e.g., is SSP a good description of our galaxies?). The magnitude of the systematic errors is unknown, and ignored in our discussions.

4.1. Self-consistency of the continua

A running mean average was subtracted from both the observed and the model spectra to minimize the influence of miscalibrations (§ 4). Then our fits are virtually blind to the galaxy continua. The question arises as whether the ages and metallicities thus derived are or not consistent with the observed galaxy continua.

In order to assign a continuum to the model spectra, one has to bring out the continuum information removed

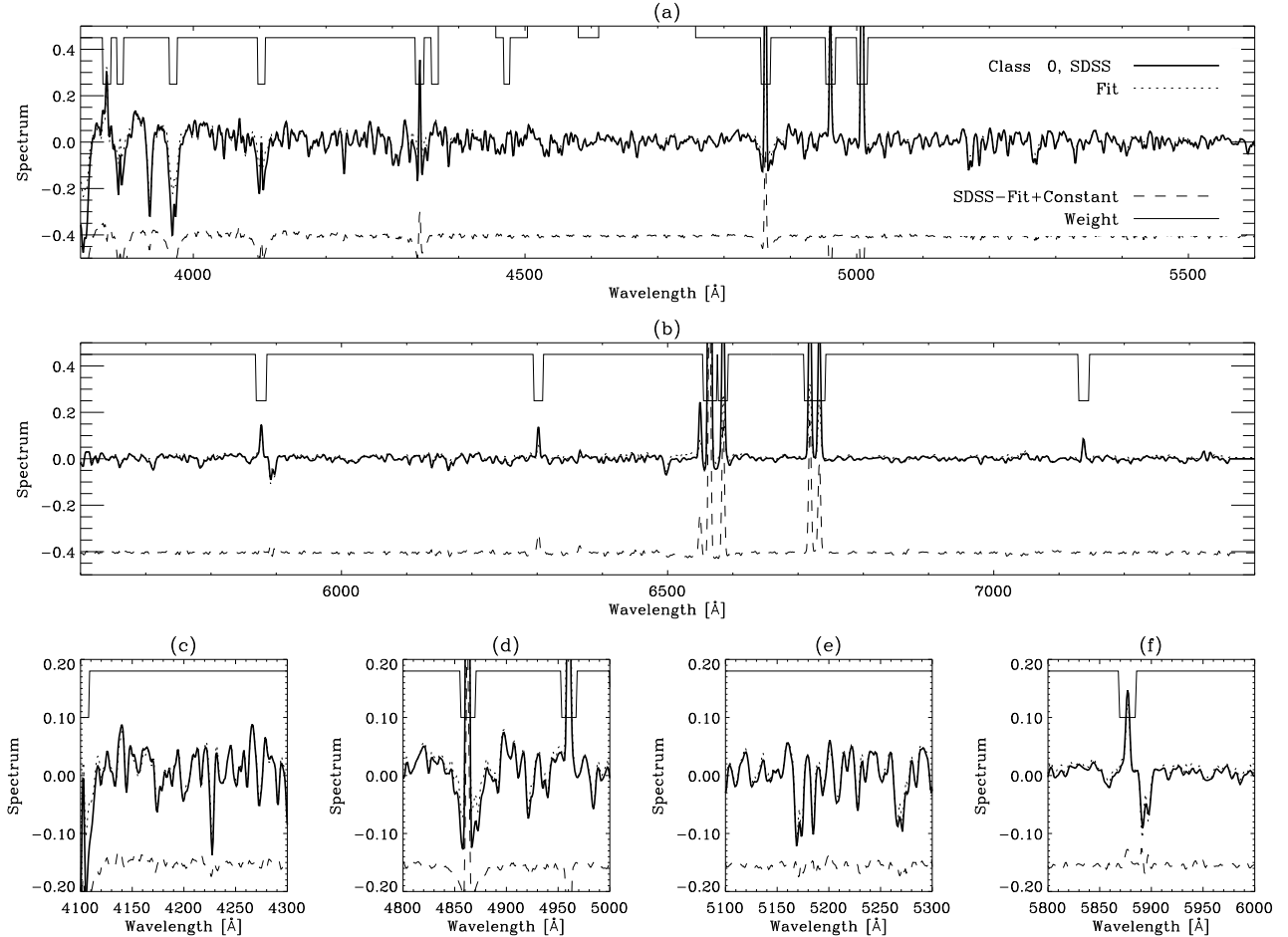


FIG. 7.— Observed average spectrum of QBCD Class 0 (the thick solid line) and best fitting MILES SSP synthetic spectrum (the dotted line). The dashed line corresponds to the residuals vertically shifted by an arbitrary amount. Panels (a) and (b) show the full spectral range, whereas (c), (d), (e) and (f) zoom into details to appreciate the goodness of the fit. The weights of the fits are represented in its own scale as a thin solid line, with the minima corresponding to no contribution, i.e., to weight equals zero. The weight goes out of scale in (a) indicating the wavelengths of the three Lick metallic indexes overweighted during fitting (Fe4383, Fe4531, and Fe4668). The continuum has been subtracted from both the observed, and the synthetic spectra.

when subtracting the running mean average. We do it by parameterizing the relationship between the actual observed spectrum, o_i , and model we fit, m_i , including the biases that the subtraction of a continuum removes, i.e.,

$$o_i = m_i 10^{-(A_i - A_0)/2.5} + \kappa_i, \quad (10)$$

where A_i corresponds to extinction by dust³ defined as usual (e.g., Cardelli et al. 1989), and κ_i accounts for other possible differences not included in the model. (Recall that the underscript i parameterizes the variation with wavelength.) Equation (10) also assumes that the model spectrum includes a gray extinction given by A_0 (incorporated into the global scaling factor β that we use for fitting; see equation [7]). As we will show, the expression (10) is fully consistent with equation (1) if one removes a running mean average of the observed spectrum, $\langle o_i \rangle$. The spectrum we fit (O_i in equation [1]) is

$$O_i = o_i - \langle o_i \rangle \simeq (\alpha N_i + \beta S_i) 10^{-(A_i - A_0)/2.5}, \quad (11)$$

³ Both internal, and due to our Galaxy, since the two of them add up when dealing with low redshift targets.

with the model galaxy spectrum given by

$$\alpha N_i + \beta S_i = m_i - \langle m_i \rangle. \quad (12)$$

We have employed equation (10) assuming that A_i and κ_i do not vary within the kernel that defines the running mean (i.e., $\langle A_i \rangle = A_i$, and $\langle \kappa_i \rangle = \kappa_i$). Neglecting in equation (11) terms of the order of,

$$(\alpha N_i + \beta S_i) (A_i - A_0), \quad (13)$$

one ends up with,

$$O_i \simeq \alpha N_i + \beta S_i, \quad (14)$$

which is the approximation used for fitting (equation [1]). Within this approximation, one can re-write equation (10) as,

$$o_i \simeq \alpha N_i + \beta S_i + \langle o_i \rangle, \quad (15)$$

where

$$\langle o_i \rangle = [1 - (A_i - A_0)/(2.5 \log e)] \langle m_i \rangle + \kappa_i, \quad (16)$$

is the term to be added to the best fitting synthetic spectrum, $\alpha N_i + \beta S_i$, to recover the observed spectrum with continuum, o_i . Equation (16) allows us to estimate both

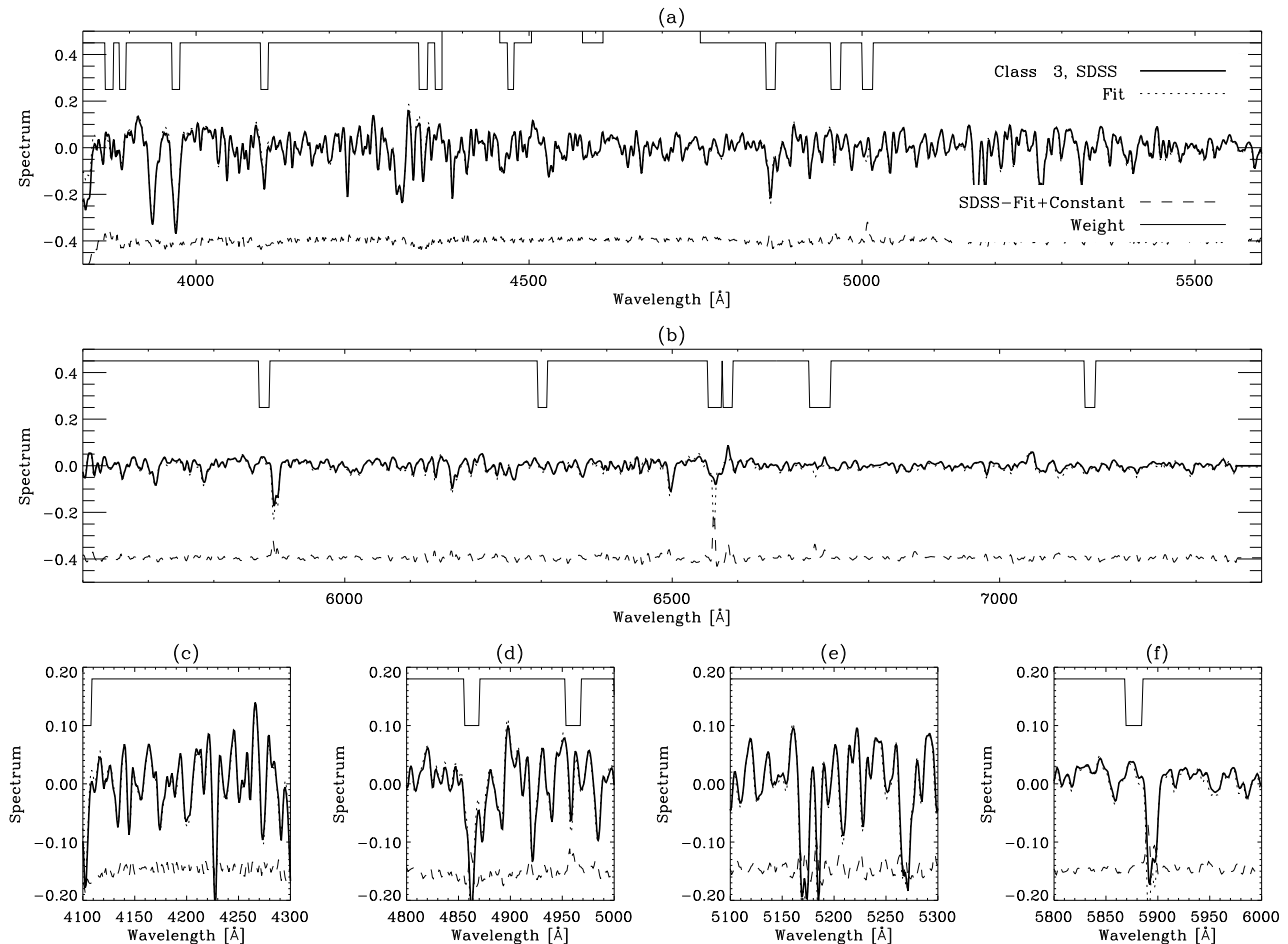


FIG. 8.— Same as Fig. 7 except that the spectrum corresponds to Class 3 QBCD, i.e., the class corresponding to the red sequence galaxies without significant emission lines.

A_i and κ_i and, consequently, to complete the best fitting model with its continuum. For lack of better assumption, we regard κ_i as independent of wavelength. In addition, the wavelength dependence of A_i is assumed to be known except for a scaling factor, parameterized as the extinction in the Johnson's V band A_V . The ratio A_i/A_V is assumed to follow the milky-way law by Cardelli et al. (1989), modified according to Misselt et al. (1999) to represent the large Magellanic cloud, which we use as a proxy for low metallicity extinction law. (The conclusions below remain even if one directly takes the milky-way extinction law.) Then the constants κ_i and A_V can be retrieved from a linear least squares fit using equations (15) and (16) since σ_i , m_i , $\langle m_i \rangle$ and A_i/A_V are all known, and one can regard A_0 as the (wavelength) average extinction. The comparison between observations and model spectra including continuum for the nine first QBCD classes is shown in Fig. 10. (The emission lines have been artificially taken out to better appreciate differences between observed and model continua.) A_V is forced to be non-negative, so that if a (small) negative number is found in an unconstrained fit, it is automatically set to zero. The agreement is good, in particular, for the most numerous classes. Keep in mind that the fitting procedure disregards continua, yet, the observed and model continua match quite well. The agreement is

found for low extinctions, of only a few tenths of magnitudes, $A_V = 0.18 \pm 0.27$. Moreover, the most populated classes are in the low extinction range of such interval, e.g., $A_V = 0.04$ for Class 0 (see the labels in Fig. 10).

4.2. Why we do not use spectra of individual galaxies to estimate ages and metallicities

Only average spectra are used in our analysis. Insufficient signal-to-noise ratio refrain us from assigning ages and metallicities to individual galaxies. The reason stands out clearly from the error budget analysis in § 4. The *rms* fluctuations of the residual of the fits are as small as 1.5% (see Figs. 7 and 8) and, even in this case, the constraint they provide are quite loose. The individual SDSS spectra have $S/N \gtrsim 4$, and this sole random error would rise the residual of any fit to an *rms* $\lesssim 25\%$. This residual is some 15 times larger than the residuals of our fits, and such a large error would make our analysis completely unreliable. One spectrum is not sufficient. Putting the same idea in other words; if the errors of the stacked spectra are similar and independent, averaging at least some $\sim 15^2 \simeq 220$ spectra is required to get the kind of residual represented in Figs. 7 and 8.

5. GAS METALLICITIES

The gas (or nebular) metallicities of the different classes of QBCDs and BCDs are estimated using

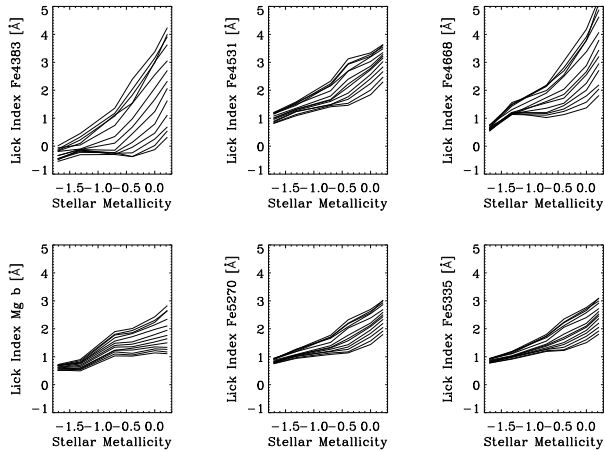


FIG. 9.— Variation with metallicity of various Lick indexes in MILES SSP spectra. Each curve of each plot corresponds to a constant age. We only show young populations, with ages between 0.5 Gyr (the curves of smallest equivalent widths) and 2 Gyr (the curves of largest equivalent widths). The wavelength range corresponding to the indexes in the top row are overweighted in our fits to break down the metallicity degeneracy. Other commonly used indexes are discarded because they present less dependence on metallicity for this range of ages; see the bottom row. The index name can be found in the ordinate axis labels. The corresponding bandpasses are defined in Worthey et al. (1994). Metallicities are given in a logarithm scale referred to the solar metallicity.

strong line empirical calibration methods. Specifically, we primarily use the so-called N2 method as provided by Pettini & Pagel (2004). We cannot employ the more accurate T_e estimate because the $[\text{OIII}]\lambda 4363$ line required to compute electron temperatures (see, e.g., Izotov et al. 2006, § 3.1) is much too faint in QBCDs. Since using strong line methods is always controversial (e.g., Stasińska 2004, 2008; Shi et al. 2005), we have studied some of the potential biases that may arise. The success of empirical calibrations resides in the agreement between the physical conditions of the calibration targets, and those of the galaxies to be analyzed. As we discuss in App. A, the calibration by Pettini & Pagel (2004) holds for a fairly large range of conditions, broad enough as to encompass the different physical conditions to be expected in QBCDs and BCDs. Moreover, the various available strong line calibrations give consistent results when applied to our spectra. If the observed differences between the metallicities of BCDs and QBCDs (Paper I, but also § 1 and the forthcoming paragraphs) were an artifact of using strong line calibrations, different calibrations should provide different biases. However, they coherently show the QBCDs to be more metallic than the BCDs. Figure 11 presents estimates based on N2 and O3N2 as calibrated by Pettini & Pagel (2004). When applied to our spectra, the two of them agree within 0.1 dex; compare the squares (N2) and the asterisks (O3N2) in Fig. 11. We have also tried with the S23 index as calibrated by Díaz & Pérez-Montero (2000), giving results similar to N2 and O3N2⁴. In short, the difference of gas metallicity between QBCDs and BCDs does not seem to be a bias caused by using the N2 method. We do not

⁴ Other methods, like P23 and P (Shi et al. 2005), cannot be applied because some of the required emission lines lie outside the spectral range of the SDSS spectra.

correct for dust extinction to derive metallicities. This approximation can be readily justified since our main calibration N2 uses two spectral lines so close in wavelength that the correction for extinction is truly negligible ($\simeq 0.0006$ dex for a one magnitude extinction). We measure the mean extinction for QBCDs to very small (§ 4.1), and Wu et al. (2008) show how the metallicity measured in a few representative BCD starbursts is not biased by extinction.

The gas metallicities thus obtained are absolute – in the end, they are based on photo-ionization modeling which relates the number of observed photons with the number of emitting atoms in the photoionized nebula (e.g., Stasińska 2004). The stellar metallicity, however, is relative to the solar metallicity. In order to compare gas and stars, the gas metallicity must be normalized to the solar value. This normalization is delicate and may bias the comparison, particularly in this moment when a major revision of the solar metallicity scale has occurred (Allende Prieto et al. 2001; Asplund 2005; Grevesse et al. 2007), and it is not consistently implemented in modeling. For this reason, we feel compelled to discuss our use of the modern oxygen abundance for gas metallicity normalization,

$$12 + \log(\text{O}/\text{H})_{\odot} = 8.66 \pm 0.05, \quad (17)$$

despite the fact that the MILES SSP spectra used in our stellar metallicity estimates are based on a stellar library whose metallicities date back to pre-revision days (Cenarro et al. 2007; Le Borgne et al. 2004; Cayrel de Strobel et al. 2001). The modification of the of solar metallicity had to do with improved modelling – NLTE effects and realistic 3D hydrodynamical model atmospheres have been incorporated into the analysis (Asplund 2005). Since the observed solar spectrum has not been modified, the revision simply re-labelled it with a different metallicity. For the sake of argumentation, assume that the spectrum of one of our galaxies has solar metallicity. Then it has the metallicity corresponding to the oxygen abundance in equation (17), rather than the metallicity originally assigned to it. Consequently, the use of MILES SSP spectra to estimate stellar metallicities is consistent with using equation (17) for the solar metallicity that normalizes the absolute gas metallicity inferred from emission lines. Table 1 lists the relative N2 gas metallicities thus computed, together with the equivalent widths of two lines used in such estimate ($\text{H}\alpha$ and $[\text{NII}]\lambda 6583$).

6. GAS METALLICITY VS STELLAR METALLICITY

In this section we compare the stellar metallicities worked out in § 4 with the gas metallicity derived from emission lines in § 5.

The scatter plot gas metallicity vs stellar metallicity is shown in Fig. 11. It includes all QBCD classes except Class 3, which has no emission lines. Several features are notable. First, the stellar metallicities of the most representative Classes (0 and 1) are systematically smaller than the nebular metallicities⁵. This result holds even when the (large) error bars of our metallicity estimates

⁵ Since these metallicities are referred to the solar value, we can directly compare the global metallicity by mass provided by the

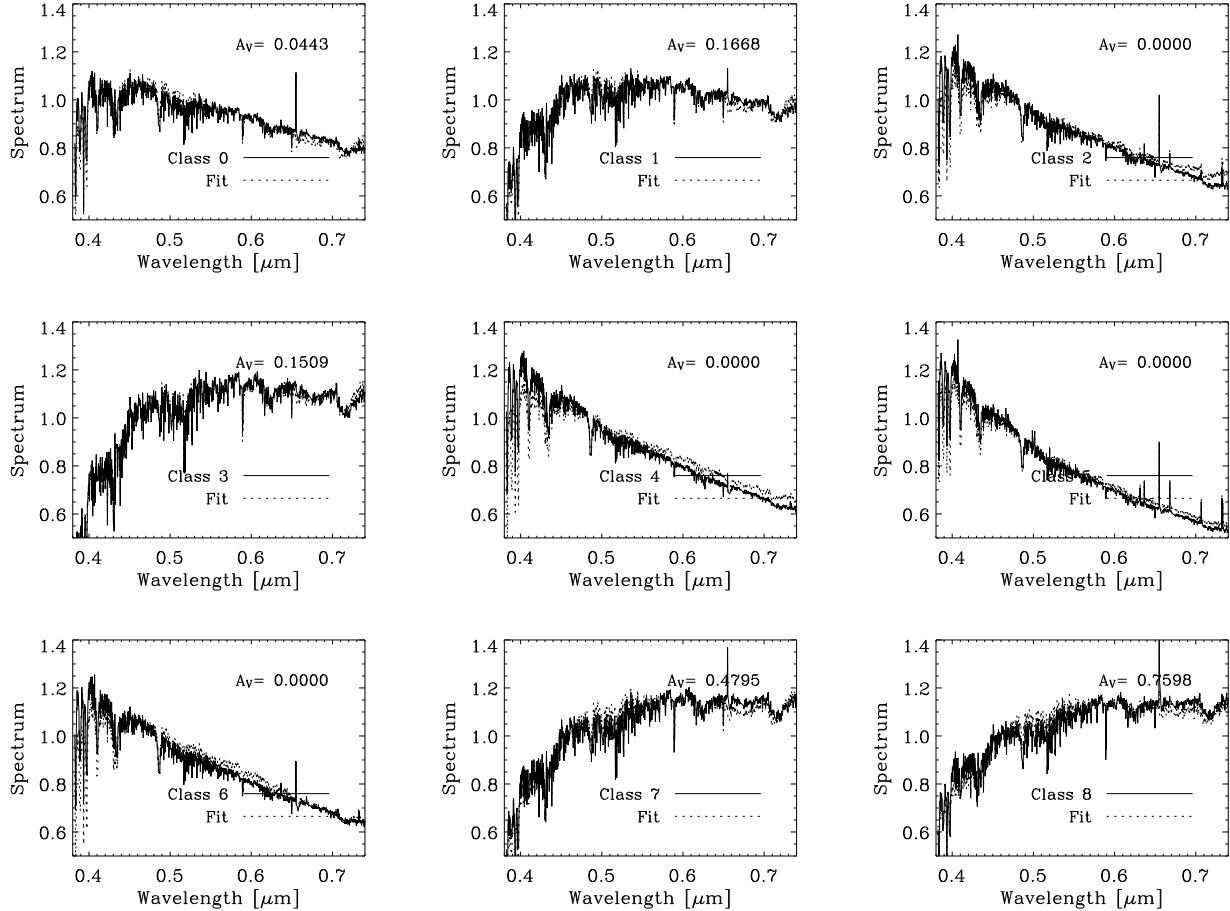


FIG. 10.— Similar to Fig. 2, except for the ordinate scale, magnified to appreciate differences between the observed continua (the solid lines), and the one inferred from fitting absorption lines (the dotted lines). The emission lines have been taken out to avoid overcrowding of the plots. The insets provide the class number of the spectrum together with the extinction coefficient A_V .

are taken into account. Figure 11 includes the error bars assigned to the metallicities of Class 0, and it is clear that the retrieved stellar and nebular metallicities disagree. The stellar metallicity error bar has been taken from the Monte Carlo simulations described in § 4, and is listed in Table 1. As for the emission line metallicity, we take 0.18 dex inferred by Pettini & Pagel (2004) from the dispersion of the N2 based metallicity when compared with the more precise T_e method. (See also App. A.) Error bars are similar for other classes. They have not been included to avoid cluttering Fig. 11, but they are listed in Table 1. Note that contrarily to the behavior of Classes 0 and 1, Classes 2 and 4 present similar stellar and nebular metallicities. This is not so much due to a change of stellar metallicity, but to a significant decrease of the nebular metallicity. The same kind of agreement at low metallicity occurs for all BCD classes. Figure 12 includes the scatter plot of nebular vs stellar metallicity for the BCD classes (the solid star symbols). Stellar and nebular metallicities agree in this case, discarding serious systematic errors biasing our conclusion. To be more precise,

spectral fitting procedure, with the oxygen metallicity by number inferred from emission lines. They correspond to the same quantity under the implicit assumption that the relative metal abundance of our targets follow the solar composition. This should be a good approximation for dwarf galaxies (e.g., Michielsen et al. 2008).

assuming that systematic errors in QBCDs and BCDs metallicities are similar, the QBCDs and the BCDs tend to have the same stellar metallicity but different nebular metallicities. Taking the most numerous Class 0 to represent them (i.e., the largest symbols with error bars in Fig. 12), the stellar metallicities Z_s of QBCDs and BCDs are similar,

$$\log(Z_s/Z_\odot)_{\text{QBCD}} \simeq \log(Z_s/Z_\odot)_{\text{BCD}}, \quad (18)$$

and also similar to the nebular metallicity of BCDs,

$$[\text{O}/\text{H}]_{\text{BCD}} \simeq \log(Z_s/Z_\odot)_{\text{BCD}}, \quad (19)$$

which differs from the nebular metallicity of QBCDs,

$$[\text{O}/\text{H}]_{\text{QBCD}} \simeq [\text{O}/\text{H}]_{\text{BCD}} + 0.35. \quad (20)$$

As usual, we have employed the notation where $[\text{O}/\text{H}] = \log(\text{O}/\text{H}) - \log(\text{O}/\text{H})_\odot$, and Z_\odot stands for the solar metallicity. Equations (18), (19), and (20) combined yield,

$$[\text{O}/\text{H}]_{\text{QBCD}} \simeq \log(Z_s/Z_\odot)_{\text{QBCD}} + 0.35. \quad (21)$$

All the above identities have an uncertainty of the order of 0.2 dex, which is large but does not invalidate the trends.

Figure 12, the dashed line, includes the relationship between nebular and stellar metallicities corresponding to a

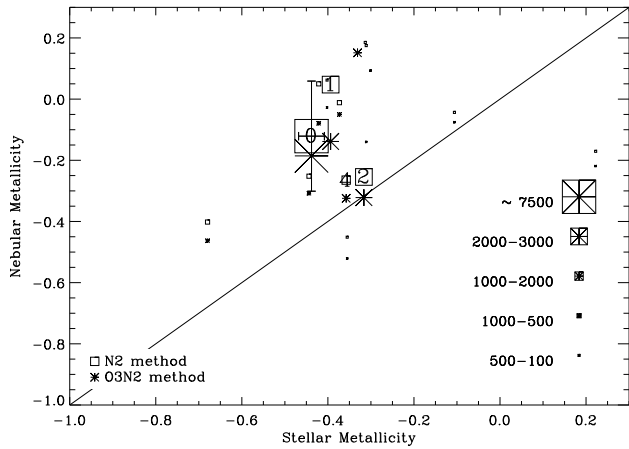


FIG. 11.— Emission line based metallicity vs stellar metallicity for the set of QBCD classes. The size of the symbol indicates the number of galaxies represented by the class, as specified in the inset. Boxes and asterisks correspond to two different estimates of emission line oxygen metallicity. The numbers inside the square symbols identify the major classes. Error bars for Class 0 are shown for reference, and they are similar to those of all major classes; see Table 1.

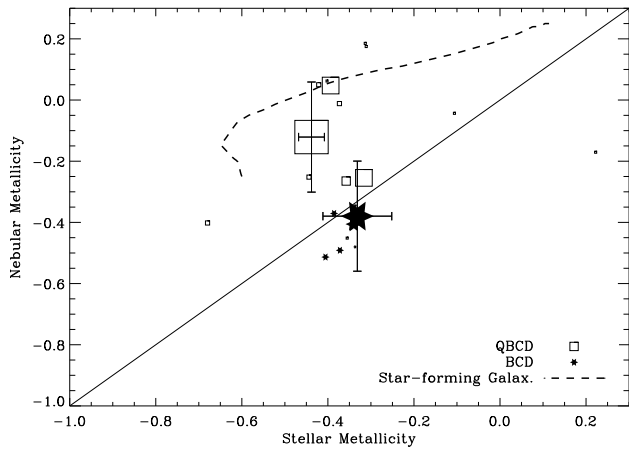


FIG. 12.— Same as Fig. 11 but for both QBCDs (the square symbols) and BCDs (the star symbols). The dashed line shows the relationship for star-forming galaxies inferred from the works of Tremonti et al. (2004) and Gallazzi et al. (2005) (see main text). The size of the symbol scales with the number of galaxies in the class. Our estimate of Class 0 error bars is shown for reference.

large set of SDSS star-forming galaxies. We have inferred such a relationship by combining the medians of the mass-metallicity relationships by Tremonti et al. (2004) and Gallazzi et al. (2005). Tremonti et al. (2004) derive metallicities from emission lines, whereas Gallazzi et al. (2005) metallicities refer to the luminosity weighted stellar metallicity. The emission line metallicities are referred to the solar metallicity using the solar oxygen abundance employed by Charlot & Longhetti (2001), which is the code behind Tremonti et al. (2004) estimates. Figure 12 shows how the nebular metallicities are systematically larger than the stellar metallicities for galaxies of the same mass, and such difference is similar to the one we find for QBCDs (equation [21]). We cite this disagreement as a consistency test for our metallicity determinations since both Tremonti et al. (2004) and

Gallazzi et al. (2005) derive metallicities using tools different and more elaborated than the ones used here. If an unknown bias is causing the differences between nebular and stellar metallicities in QBCDs, it does not seem to be due to our specific simplifying hypotheses.

The error bars employed so far correspond to 1σ , or 68% confidence level. If we use 2σ instead, we cannot discard the agreement between the gas and the stellar metallicities of QBCDs (in the case of N2 based nebular metallicities, $2\sigma \simeq 0.41$ dex; Pettini & Pagel 2004). Note, however, that the error bars used for the nebular metallicity are rather conservative. We find that the metallicities inferred from O3N2 and N2 agree (§ 5 and Fig. 11), and the scatter of the O3N2 relationship found by Pettini & Pagel (2004) is significantly smaller than that of N2 method ($2\sigma \simeq 0.25$ dex for O3N2). Moreover, the scatter found by Pettini & Pagel (2004) corresponds to individual extragalactic H II regions. Part of such scatter have to be of random nature, and it cancels when averaging many different regions or, as we do, many different galaxies. Only the (unknown) systematic part of the error would be of relevance in our case.

7. AGE OF THE STELLAR COMPONENT

The absorption line spectrum fitting procedure in § 4 provides ages and metallicities for the stellar component of the galaxies. Figure 13 shows the metallicity vs age scatter plot corresponding to the two sets of galaxies, QBCDs and BCDs. We find that QBCDs are systematically older than BCDs. QBCDs have ages in excess of 1 Gyr whereas all BCDs have ages inferior to (but close to) 1 Gyr. The case of QBCD Class 3 is worthwhile mentioning separately (the oldest age in Fig. 13, of the order of 11 Gyr). It corresponds to the QBCD galaxies without emission lines (Fig. 2), which form the red clump of the color sequence (Fig. 5). These properties hint at Class 3 being early type galaxies, and the age we find is also consistent with this possibility. Such a very old origin of the stellar population of Class 3 is very well constrained according to our error analysis – see Table 1.

According to the conjecture we are examining in the paper (§ 1), QBCDs undergo successive starbursts that transform then to BCDs for short periods (lasting only 10 Myr or so; see, e.g., Mas-Hesse & Kunth 1999). The number density of BCDs and QBCDs requires the bursting phase to appear, statistically, every 0.3 Gyr. The fact that this timescale differs from the age we assign to the QBCDs is not at odds with the conjecture. The stellar population we observe now has been produced not just during the last starburst, but during several bursts. It is the luminosity weighted age of these populations what we have estimated, which has to exceed the age of the last starburst. The fact that the age of the stellar population of BCDs is shorter but not very different from the age of QBCDs adds on to this picture. If BCDs and QBCDs are basically the same galaxies, but the BCDs happen to be in a phase of enhanced star formation activity, then the underlying stellar populations must have similar properties. This turns out to be the case. The metallicities are similar (§ 6 and equation [18]), and BCD stellar ages are shortened due to the strength of the current starburst.

The fact that the age of the stellar population of BCDs is much larger than the age of a typical starburst supports that BCD are not forming stars for the first time.

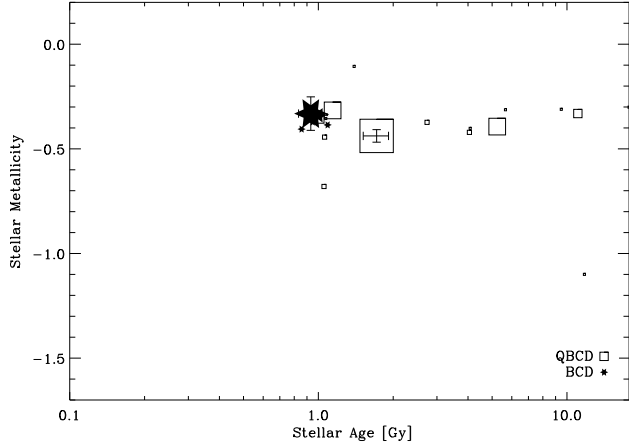


FIG. 13.— Stellar metallicity vs stellar age scatter plot for both QBCDs (the square symbols) and BCDs (the solid star symbols). Error bars for Class 0 QBCDs and BCDs are included. The size of the symbols codes the number of galaxies in the class, like in Fig. 11. The range of the axes corresponds to the full range of ages and metallicities spanned by the MILES SSP library. Note how the assigned ages and metallicities occupy a well-defined narrow region among of the possible solutions.

They have an underlying stellar population much older than a starburst.

8. METAL ENRICHMENT AND STAR FORMATION

This section analyzes the difference between the observed nebular and stellar metallicities of QBCDs. We will find that the nebular metallicity of QBCDs seems to be much too high to be representative of the galaxy as a whole. Should it be representative, the QBCD galaxies would have been forming stars during the last few Gyr at an unobservedly large SFR. As we conjectured in Paper I, the metallicity of QBCDs inferred from emission lines probably represents a small fraction of the galactic gas, locally contaminated by recent starbursts.

In principle, the difference between stellar metallicity and gas metallicity found in § 6 may be explained in terms of the chemical enrichment of the ISM during the time span between the formation of the stars and the present epoch. Assume that the chemical enrichment has followed a closed-box evolution. (The consequences of an open-box evolution will be discussed later on.) In this case the conservation of metals imposes the following constraint between the mass of stars M_s , the mass of gas M_g , the metallicity of the stars Z_s , the metallicity of the gas Z , and the yield y ,

$$Z M_g + Z_s M_s = y M_s + Z_0 M. \quad (22)$$

(We will use without explicit citation well known results from the theory of chemical evolution of galaxies; see, e.g. Tinsley 1980; Pagel 1997.) The left hand side of equation (22) gives the amount of metals now existing in stars and gas, which is equal to the metals created by stars, $y M_s$, plus the metals existing at the beginning of the starburst, $Z_0 M$, where M stands for the total mass in the star-forming closed-box, and Z_0 represents the initial metallicity of the gas. Equation (22) can be rewritten in a more convenient form,

$$\mu = \frac{y + Z_0 - Z_s}{y + Z - Z_s}, \quad (23)$$

with μ the mass fraction of gas,

$$\mu = M_g/M. \quad (24)$$

Also from the theory of closed-box evolution,

$$Z - Z_0 = -y \ln \mu, \quad (25)$$

and

$$\mu = 1 - \frac{(1 - R) \text{SFR} t}{M}, \quad (26)$$

with SFR the average Star Formation Rate during the past time interval t , and R the fraction of stellar mass that returns to the ISM rather than being locked into stars and stellar remnants. Equations (23) and (25) combined provide the difference of metallicity between gas and stars,

$$Z - Z_s = -y \left[\frac{\ln \mu}{1 - \mu} + 1 \right]. \quad (27)$$

In principle, the mass of the starburst M is unknown, but our ignorance can be parameterized using a scaling factor f between M and the mass of stars in the galaxy at present M_* , i.e.,

$$M = f M_*. \quad (28)$$

Although it is not a primary observable, the stellar mass content of a galaxy can be inferred from its observed luminosity and color. Using the calibration modeled by Bell & de Jong (2001), the color transformations between Johnson's colors and SDSS colors by Jester et al. (2005), and the typical colors of the QBCD candidates in Paper I, one finds a relationship between the stellar mass in solar mass units, and the absolute magnitude in the SDSS g color,

$$\log(M_*/M_\odot) \simeq -0.50 g + 0.35. \quad (29)$$

The parameters R and y are constrained by the stellar evolution models, so that $R \simeq 0.2$ (e.g., Tinsley 1980; Pagel 1997; Aparicio & Gallart 2004) and, for oxygen, $y \simeq 4 \times 10^{-3}$ (Dalcanton 2007, and references therein). Then given the age, the SFR, and the mass (i.e., f) of a starburst, equations (26), (27) and (28) allows us to predict the difference of metallicity between gas and stars, which is the parameter measured in § 6. Consequently, we can use them to estimate the mass of the starburst and/or the SFR required to explain the observed metal enrichment of the gas. This is what we do next.

One can estimate the present SFR of the QBCD galaxies from their $H\alpha$ emission. We have used the prescription in Kennicutt (1998), which gives the SFR as a function of the $H\alpha$ luminosity. We derive the luminosity from the observed $H\alpha$ equivalent width, and the absolute luminosity of the galaxies in the SDSS r bandpass, approximately centered at the $H\alpha$ wavelength. The transformation between magnitudes and fluxes has been carried out keeping in mind that the SDSS color system is an AB system (Smith et al. 2002), which renders,

$$\text{SFR} \simeq \gamma \frac{W_{H\alpha}}{100 \text{ \AA}} 10^{-0.4(r+19.0)} M_\odot \text{ yr}^{-1}, \quad (30)$$

with $W_{H\alpha}$ the equivalent width in \AA , r the integrated absolute r magnitude, and γ the fraction of galactic

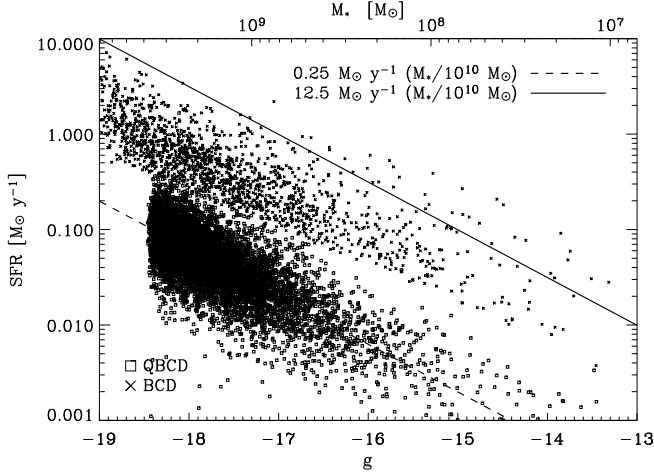


FIG. 14.— Star Formation Rate (SFR) vs SDSS g absolute magnitude. Both QBCD galaxies (Class 0; the square symbols) and BCD galaxies (full set; the times symbols) are included. The dashed line represents the average QBCD SFR, i.e., $\text{SFR} \simeq 0.25 \cdot (M_*/10^{10} M_\odot)$. The solid line corresponds to a SFR 50 times larger. The stellar mass of the QBCD galaxies derived from the g magnitude is also included in the scale on top of the figure.

light contributing to the the starburst.⁶ Figure 14 shows the SFRs inferred from equation (30) for the individual QBCD galaxies in Class 0 (the square symbols). We have used $\gamma = 0.5$, as a reasonable upper limit for the extent of the starburst, but using 0.1 or 1 do not change any of the conclusions discussed below. Typically, the SFR is $0.1 M_\odot \text{y}^{-1}$ for the brightest QBCDs, i.e., when $g \simeq -18.5$. Figure 14 also includes the SFR of BCDs – in this case $\gamma = 1$ to acknowledge that the starburst is spread out all over the galaxy.

Figure 15 shows the difference between nebular and stellar oxygen metallicities predicted by the closed-box evolution of Class 0 QBCD galaxies. We assume t to be the age of the stellar population derived in § 7. Equations (26), (27), (28), (29), and (30) were used with $f = 2$ (the square symbols) and $f = 0.04$ (the times symbols). The case $f = 2$ represents a galaxy-wide starburst able to pollute with metals the whole galactic gas. ($f = 2$ assumes the same amount of mass in gas as the mass in stars, which is reasonable for low surface brightness dwarf galaxies like our QBCDs. According to Staveley-Smith et al. (1992), they have one M_\odot of HI gas per solar luminosity, which corresponds to $f \simeq 3$.) In this case the predicted difference of metallicity is too low to account for the observed difference (§ 6), which is represented in Figure 15 as a horizontal solid line. The amount of metals produced at the current SFR during the age of the starburst is insufficient to effectively contaminate the whole ISM of the galaxies. If, on the other hand, the same starburst pollutes only a small fraction of the galactic gas ($f = 0.04$, or a factor 50 smaller than the previous case), then the predicted and the observed metallicities agree (Fig. 15, the times symbols). Con-

⁶ Note that the SDSS equivalent width corresponds to a spectrum taken at the center of the galaxy (§ 2). Using the integrated luminosities to estimate $H\alpha$ fluxes assumes that the star-forming burst observed at the galaxy core extends evenly throughout the galaxy. The factor γ accounts for the case where the starburst affects only a fraction γ of the galaxy.

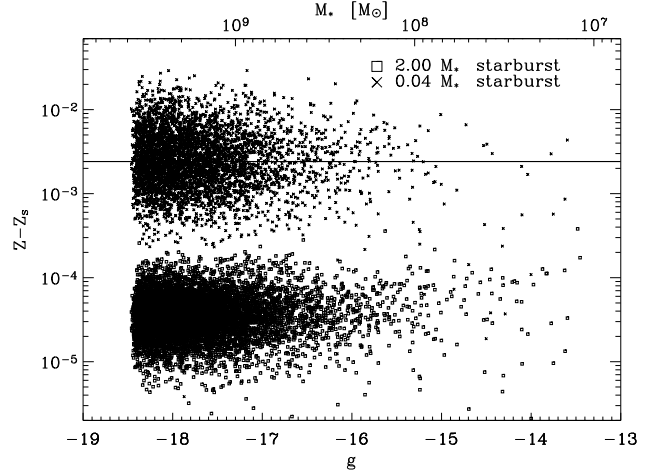


FIG. 15.— Difference between nebular and stellar metallicities ($Z - Z_s$) predicted if the chemical evolution of Class 0 QBCDs follows a closed-box model. The difference is plotted vs the absolute g -color magnitude (bottom axis) and vs the stellar mass of the galaxy (M_* , top axis). The horizontal solid line corresponds to the observed difference, which can be reproduced only if a small fraction of the galactic gas is polluted with metals (see the main text).

sequently, the observed $Z - Z_s$ can be explained if the gas from which we infer the metallicity represents only a small fraction of the total galactic gas.

Agreement between observed and model metallicities can be also reached if the QBCD galaxies had an average SFR during t much larger than the present one. The predicted closed-box evolution depends on the ratio SFR/f rather than on SFR and f separately, and a decrease of f is equivalent to an increase of SFR; see equations (26) and (28). However, the required increase of SFR is too high to be sensible. It would have to be 50 times larger than the observed ones. This level of *continuous* star formation activity during the last two Gyr is unreasonably high; it is shown as a solid line in Fig. 14 and it corresponds to $\sim 5 M_\odot \text{y}^{-1}$ for the brightest QBCD galaxies. It is larger than the already large SFR observed in our BCD galaxies (see Fig. 14, the times symbols).

So far our argumentation has considered closed-box chemical evolution. If the box is opened both infall of (low metallicity) gas from the intergalactic medium, and outflows of metal rich SNa ejecta are to be expected (e.g., Garnett 2002; Dalcanton 2007, and references therein), and both processes reduce the metallicity of the gas with respect to the predictions of the closed-box model. Then it becomes even more difficult explaining the observation as a global chemical enrichment. An approximate way of considering this open-box evolution using closed-box equations consists of using effective yields inferred from observations rather than the yield predicted by stellar evolution models (e.g. Dalcanton 2007). These effective yields are smaller than true yields, and the difference increases with decreasing galaxy mass (probably due to the decrease of the gravitational potential of the galaxy). Actually, the deviations are particularly large for dwarf galaxies, like our QBCDs (e.g., Garnett 2002; Dalcanton 2007). If the yield y is reduced, then $Z - Z_s$ decreases too – see equation (27) and keep in mind that μ is fixed by equation (26). In short, the assumption of closed-box chemical evolution do not invalidate our conclusion,

namely, that the metallicity we infer from the emission lines traces only a small fraction of the total galactic gas.

So far we have put aside the behavior of the BCDs. According to Fig. 12, they have the same nebular and stellar metallicities within error bars. In addition, the stellar populations have ages slightly smaller than 1 Gyr (Fig. 13). These two properties can be easily explained if the BCD galaxies are QBCDs experiencing a major but short starburst involving fresh well mixed galactic gas. In this case, the observed BCD SFR is significantly larger than the average SFR during the age of the stellar population. Then the chemical evolution model to be applied has $M \sim M_*$, and a SFR of the order of the SFR of QBCDs, i.e., a model similar to the case labelled as $2M_*$ in Fig. 15. The model prediction is $Z - Z_s$ at least one order of magnitude smaller than the difference observed in QBCDs and, therefore, in agreement with the lack of metal enrichment observed in BCDs (the stars in Fig. 12).

9. CONCLUSIONS

We analyze the metallicity of QBCDs, i.e., galaxies that may be Blue Compact Dwarfs (BCDs) during the periods of quiescence, when the major starburst characteristic of BCDs is not so dominant. The QBCD candidates were selected in Paper I from SDSS/DR6, where we also separate a reference sample of BCDs. The metallicity inferred from emission lines of these QBCDs turned out to exceed the metallicity of the BCDs, an uneasy result if BCDs have to descend from QBCDs. Here we study whether the metallicity inferred from the emission lines of QBCDs may not be representative of the full galactic gas, but reveals a local enrichment by recent starbursts. In this case the metallicities for the gas and for the stars must differ significantly.

The work is based on SDSS/DR6 spectra, whose signal-to-noise ratio is not sufficient to measuring stellar metallicities from absorption lines of individual spectra. We improve the original signal-to-noise ratio by stacking observed spectra that are alike. The grouping of similar spectra was carried out by classifying the 21493 QBCD galaxies using an automatic *k-means* classification procedure (§ 3). The algorithm renders a small number of types of spectra or *classes*, with the first ten classes containing 90% of all spectra, and the most numerous Class 0 having more than 36% of them. As a by-product, this classification scheme provides a selective technique to identify galaxies in various states within the color sequence. In particular, one of our classes seems to contain only transition galaxies in the so-called *green valley* (Class 1, § 3.1), whereas another class includes most of the red sequence galaxies (Class 3; § 3.1). The typical Class 0 QBCD galaxies belong to the blue sequence. So do BCD galaxies.

The stellar metallicities have been derived from the absorption lines using an ad-hoc procedure which fits the average profile of each class with single-stellar populations synthetic spectra based on the stellar library MILES (§ 4). We develop our own simple but robust tool to get a intuitive control of the errors. Emission lines are masked out. The galactic continuum is also subtracted for fitting, so that only absorption line features contribute to the measurement. As inferred from our Monte-Carlo estimate of the random error budget, a

direct fit of the full spectrum is good enough to assign ages, but it does not provide enough finesse to properly distinguish metallicities. Only after overweighting particular bandpasses of the stacked spectra (corresponding to some of the Lick indexes defined by Worthey et al. 1994), we bring the formal error bars down to reasonable limits, below 0.1 dex. Gas metallicities are obtained from emission lines with errors smaller than 0.2 dex (§ 5 and App. A). When the gas and the stellar QBCD metallicities are compared, gas metallicities turn out to be systematically larger than the stellar metallicities by some ~ 0.35 dex (§ 6). Despite the fact that this difference is not far from the formal error bars (actually, it is below the formal 2σ level; § 6), we regard it as significant for a number of reasons. First, it is systematic, so that the main QBCD classes show it. Second, it is not present in BCDs, where stars and gas show the same metallicity within error bars (Fig. 11). Third, the excess of gas metallicity with respect to stellar metallicity is implicit in the luminosity-metallicity relationships for star-forming galaxies inferred by Tremonti et al. (2004, gas) and Gallazzi et al. (2005, stars) (see § 6, and the dashed line in Fig. 12). Despite the existence of all these supportive arguments, a caveat is in order. The stellar metallicity error bars only describe statistical errors, although systematic errors may dominate the error budget. Even if these systematic errors exist and are important, they should not modify the conclusions as they would affect both QBCDs and BCDs in the same way. However, one can never discard a source of (unknown and unsuspected) systematic errors affecting QBCDs and BCDs differently, which would force us to reconsider the metallicity discrepancies.

The fraction of QBCD galactic light produced by stars augment with the metallicity, so that the fainter the emission lines the more metal rich the gas. This result reinforces the conjecture that the emission lines come from self enriched ISM. The luminosity weighted ages of QBCDs span the full range from 1 to 10 Gyr (Fig. 13). The most common Class 0 is in the young part of such range, with an age below 2 Gyr. The fact that the age of the stellar population of BCDs is shorter but not very different from the age of QBCDs adds on to this picture. If BCDs and QBCDs are basically the same galaxies, but the BCDs happen to be in a phase of enhanced star formation activity, then the underlying stellar populations must have similar properties. Their stellar metallicities are similar (§ 6). The BCD ages are smaller than the QBCDs ages, but this can be easily due to the fact that their luminosity weighted average ages are reduced by the current starburst.

In principle, the excess of metals in the ionized gas of QBCDs, as revealed by their emission lines, may reflect the natural enrichment of the ISM produced by successive SN ejecta. Emission lines trace the present ISM, whereas stars sample it in the past when the metallicity was lower. The relative enrichment depends on the age of the stars, and also on the star formation rate providing the SNe. In the case of our QBCDs, these two quantities are tightly constrained. We have estimated the (mean) age of the starburst, and the (current) star formation rate (SFR) as inferred from the observed $H\alpha$ luminosity (Kennicutt 1998). Using simple closed-box chemical evolution models, we argue that given the age

and the star-formation rate, the observed starburst is not sufficient to enrich the full galactic ISM to the observed levels. However, age and SFR can be accommodated if the enriched galactic gas represents only a small fraction of the total gas ($\sim 1/50$; § 8). The assumption of closed-box evolution does not invalidate the conclusion.

As we point out in Paper I, QBCD are quiet common, representing one out each three dwarf galaxies in the local universe. Since they are so common, it is conceivable that some of their properties are not exclusive of the QBCD class, but a global property of dwarf galaxies with emission lines. In particular, the bias of metallicity inferred from emission lines may be present in all star-forming dwarf galaxies, rather than being a feature of our particular subset. We plan to explore this potential bias using the techniques developed in the paper, namely, the comparison between the metallicity estimates based on emission lines and absorption lines. Moreover, we plan of applying the classification tool in § 3 to find out and characterize galaxy spectra corresponding to the various parts of the color sequence. The short green-valley phase is particularly interesting (e.g., Dellenbusch et al. 2007; Silverman et al. 2008), and we came across a simple method of identification.

Thanks are due to B. Panter for clarifying discussions on the proper solar abundance normalization to be used with Tremonti et al. (2004) relationship. Thanks are also due to an anonymous referee for helping us improving the argumentation. We benefitted from comments and suggestions by R. Amorín, I. G. de la Rosa, C. Esteban, A. Manpaso, M. Mollá, E. Pérez-Montero, R. Sánchez-

Janssen, G. Stasińska, and J. Vílchez on aspects of this paper related to their area of expertise. This work has been partly funded by the Spanish *Ministerio de Educación y Ciencias*, projects AYA 2007-67965-03-01 and AYA 2007-67752-C03-01.

Funding for the Sloan Digital Sky Survey (SDSS) and SDSS-II has been provided by the Alfred P. Sloan Foundation, the Participating Institutions, the National Science Foundation, the U.S. Department of Energy, the National Aeronautics and Space Administration, the Japanese Monbukagakusho, and the Max Planck Society, and the Higher Education Funding Council for England. The SDSS Web site is <http://www.sdss.org/>. The SDSS is managed by the Astrophysical Research Consortium (ARC) for the Participating Institutions. The Participating Institutions are the American Museum of Natural History, Astrophysical Institute Potsdam, University of Basel, University of Cambridge, Case Western Reserve University, The University of Chicago, Drexel University, Fermilab, the Institute for Advanced Study, the Japan Participation Group, The Johns Hopkins University, the Joint Institute for Nuclear Astrophysics, the Kavli Institute for Particle Astrophysics and Cosmology, the Korean Scientist Group, the Chinese Academy of Sciences (LAMOST), Los Alamos National Laboratory, the Max-Planck-Institute for Astronomy (MPIA), the Max-Planck-Institute for Astrophysics (MPA), New Mexico State University, Ohio State University, University of Pittsburgh, University of Portsmouth, Princeton University, the United States Naval Observatory, and the University of Washington.

Facilities: Sloan (DR6, spectra)

REFERENCES

- Adelman-McCarthy, J. K., Agüeros, M. A., Allam, S. S., et al. 2008, *ApJS*, 175, 297
- Allende Prieto, C., Lambert, D. L., & Asplund, M. 2001, *ApJ*, 556, L63
- Amorín, R. O., Aguerri, J. A. L., Muñoz-Tuñón, C., & Cairós, L. M. 2009, *A&A*, in press, arXiv:0903.2861
- Amorín, R. O., Muñoz-Tuñón, C., Aguerri, J. A. L., Cairós, L. M., & Caon, N. 2007, *A&A*, 467, 541
- Aparicio, A. & Gallart, C. 2004, *AJ*, 128, 1465
- Asplund, M. 2005, *ARA&A*, 43, 481
- Balogh, M. L., Baldry, I. K., Nichol, R., et al. 2004, *ApJ*, 615, L101
- Bell, E. F. & de Jong, R. S. 2001, *ApJ*, 550, 212
- Bromm, V. & Larson, R. B. 2004, *ARA&A*, 42, 79
- Cairós, L. M., Vílchez, J. M., González Pérez, J. N., Iglesias-Páramo, J., & Caon, N. 2001, *ApJS*, 133, 321
- Caon, N., Cairós, L. M., Aguerri, J. A. L., & Muñoz-Tuñón, C. 2005, *ApJS*, 157, 218
- Cardelli, J. A., Clayton, G. C., & Mathis, J. S. 1989, *ApJ*, 345, 245
- Cattaneo, A., Dekel, A., Devriendt, J., Guiderdoni, B., & Blaizot, J. 2006, *MNRAS*, 370, 1651
- Cayrel de Strobel, G., Soubiran, C., & Ralite, N. 2001, *A&A*, 373, 159
- Cenarro, A. J., Peletier, R. F., Sánchez-Blázquez, P., et al. 2007, *MNRAS*, 374, 664
- Charlot, S. & Longhetti, M. 2001, *MNRAS*, 323, 887
- Cowie, L. L., Songaila, A., Hu, E. M., & Cohen, J. G. 1996, *AJ*, 112, 839
- Dalcanton, J. J. 2007, *ApJ*, 658, 941
- Davies, J. I. & Phillipps, S. 1988, *MNRAS*, 233, 553
- de Avillez, M. A. & Mac Low, M.-M. 2002, *ApJ*, 581, 1047
- Dellenbusch, K. E., Gallagher, III, J. S., & Knezek, P. M. 2007, *ApJ*, 655, L29
- Denicoló, G., Terlevich, R., & Terlevich, E. 2002, *MNRAS*, 330, 69
- Díaz, A. I. & Pérez-Montero, E. 2000, *MNRAS*, 312, 130
- Diemand, J., Kuhlen, M., & Madau, P. 2007, *ApJ*, 657, 262
- Dyson, J. E. & Franco, J. 2000, in *Encyclopedia of Astronomy and Astrophysics*, ed. P. Murdin (Bristol: Nature Publishing Group)
- Ellison, S. L., Songaila, A., Schaye, J., & Pettini, M. 2000, *AJ*, 120, 1175
- Everitt, B. S. 1995, *Cluster Analysis* (London: Arnold)
- Gallazzi, A., Charlot, S., Brinchmann, J., White, S. D. M., & Tremonti, C. A. 2005, *MNRAS*, 362, 41
- Garnett, D. R. 2002, *ApJ*, 581, 1019
- Gil de Paz, A. & Madore, B. F. 2005, *ApJS*, 156, 345
- Gil de Paz, A., Madore, B. F., & Pevunova, O. 2003, *ApJS*, 147, 29
- González, J. J. 1993, PhD thesis, University of California, Santa Cruz
- Graves, G. J., Faber, S. M., & Schiavon, R. P. 2009, *ApJ*, 693, 486
- Grevesse, N., Asplund, M., & Sauval, A. J. 2007, *Space Sci. Rev.*, 130, 105
- Izotov, Y. I., Stasińska, G., Meynet, G., Guseva, N. G., & Thuan, T. X. 2006, *A&A*, 448, 955
- Izotov, Y. I., Thuan, T. X., & Guseva, N. G. 2005, *ApJ*, 632, 210
- Izotov, Y. I., Thuan, T. X., & Stasińska, G. 2007, *ApJ*, 662, 15
- Jester, S., Schneider, D. P., Richards, G. T., et al. 2005, *AJ*, 130, 873
- Kauffmann, G., Heckman, T. M., White, S. D. M., et al. 2003, *MNRAS*, 341, 54
- Kennicutt, R. C. 1998, *ARA&A*, 36, 189
- Koleva, M., Prugniel, P., Ocvirk, P., Le Borgne, D., & Soubiran, C. 2008, *MNRAS*, 385, 1998
- Kunth, D. & Östlin, G. 2000, *A&A Rev.*, 10, 1
- Kunth, D. & Sargent, W. L. W. 1986, *ApJ*, 300, 496
- Le Borgne, D., Rocca-Volmerange, B., Prugniel, P., et al. 2004, *A&A*, 425, 881
- Loose, H.-H. & Thuan, T. X. 1986, *ApJ*, 309, 59
- Mas-Hesse, J. M. & Kunth, D. 1999, *A&A*, 349, 765
- Michielsen, D., Boselli, A., Conselice, C. J., et al. 2008, *MNRAS*, 385, 1374
- Misselt, K. A., Clayton, G. C., & Gordon, K. D. 1999, *ApJ*, 515, 128

- Moore, D. S., McCabe, G. P., Duckworth, W. M., & Sclove, S. L. 2003, *The practice of business statistics: using data for decisions* (New York: W. H. Freeman and Co)
- Noeske, K. G., Papaderos, P., Cairós, L. M., & Fricke, K. J. 2003, *A&A*, 410, 481
- Pagel, B. E. J. 1997, *Nucleosynthesis and Chemical Evolution of Galaxies* (Cambridge: CUP)
- Papaderos, P., Loose, H.-H., Fricke, K. J., & Thuan, T. X. 1996a, *A&A*, 314, 59
- Papaderos, P., Loose, H.-H., Thuan, T. X., & Fricke, K. J. 1996b, *A&AS*, 120, 207
- Pettini, M. & Pagel, B. E. J. 2004, *MNRAS*, 348, L59
- Salim, S., Rich, R. M., Charlot, S., et al. 2007, *ApJS*, 173, 267
- Sánchez Almeida, J., Muñoz-Tuñón, C., Amorin, R., et al. 2008, *ApJ*, 685, 194
- Sánchez-Blázquez, P., Peletier, R. F., Jiménez-Vicente, J., et al. 2006, *MNRAS*, 371, 703
- Sargent, W. L. W. & Searle, L. 1970, *ApJ*, 162, L155
- Searle, L. & Sargent, W. L. W. 1972, *ApJ*, 173, 25
- Shi, F., Kong, X., Li, C., & Cheng, F. Z. 2005, *A&A*, 437, 849
- Silk, J., Wyse, R. F. G., & Shields, G. A. 1987, *ApJ*, 322, L59
- Silverman, J. D., Mainieri, V., Lehmer, B. D., et al. 2008, *ApJ*, 675, 1025, revise
- Smith, J. A., Tucker, D. L., Kent, S., et al. 2002, *AJ*, 123, 2121
- Springel, V., Di Matteo, T., & Hernquist, L. 2005, *ApJ*, 620, L79
- Stasińska, G. 2004, in *Cosmochemistry. The melting pot of the elements*, ed. C. Esteban, R. García López, A. Herrero, & F. Sánchez (Cambridge: CUP), 115
- Stasińska, G. 2008, in *IAU Symposium, Vol. 255, Low Metallicity Star Formation: From the First Stars to Dwarf Galaxies*, ed. L. Hunt, S. Madden, & R. Schneider (Cambridge: CUP), 375
- Staveley-Smith, L., Davies, R. D., & Kinnan, T. D. 1992, *MNRAS*, 258, 334
- Stoughton, C., Lupton, R. H., Bernardi, M., et al. 2002, *AJ*, 123, 485
- Telles, E. & Terlevich, R. 1997, *MNRAS*, 286, 183
- Tenorio-Tagle, G. 1996, *AJ*, 111, 1641
- Thomas, D., Maraston, C., & Bender, R. 2003, *MNRAS*, 343, 279
- Thuan, T. X. 1991, in *Massive Stars in Starbursts*, ed. C. Leitherer, N. Walborn, T. Heckman, & C. Norman (Cambridge: Cambridge University Press), 183
- Thuan, T. X., Bauer, F. E., Papaderos, P., & Izotov, Y. I. 2004, *ApJ*, 606, 213
- Tinsley, B. M. 1980, *Fundam. Cosmic Phys.*, 5, 287
- Trager, S. C., Worthey, G., Faber, S. M., Burstein, D., & Gonzalez, J. J. 1998, *ApJS*, 116, 1
- Tremonti, C. A., Heckman, T. M., Kauffmann, G., et al. 2004, *ApJ*, 613, 898
- Vazdekis, A. 1999, *ApJ*, 513, 224
- Vazdekis, A. & Arimoto, N. 1999, *ApJ*, 525, 144
- White, S. D. M. & Frenk, C. S. 1991, *ApJ*, 379, 52
- Worthey, G. 1994, *ApJS*, 95, 107
- Worthey, G., Faber, S. M., Gonzalez, J. J., & Burstein, D. 1994, *ApJS*, 94, 687
- Worthey, G. & Ottaviani, D. L. 1997, *ApJS*, 111, 377
- Wu, Y., Bernard-Salas, J., Charmandaris, V., et al. 2008, *ApJ*, 673, 193

APPENDIX

RANGE OF PHYSICAL CONDITIONS WHERE N2 HOLDS

The strong-line index abundance estimates are calibrated against T_e methods using particular sets of targets (e.g., Díaz & Pérez-Montero 2000; Pettini & Pagel 2004). There is no guarantee that such calibrations hold when applied to galaxies whose physical conditions deviate from those used for calibration. In particular, if the physical conditions prevailing in the H II nebulae of QBCDs and BCDs are not included among the calibration targets, then the metallicity difference between BCDs and QBCDs found by Sánchez Almeida et al. (2008) may be an artifact of using the strong-line N2 method. The physical conditions in the BCD H II regions (newborn) and in the QBCDs H II regions (aging) are expected to differ systematically which, coupled with an unfit N2 calibration, may give rise to a false difference. Fortunately, such potential bias seems to be harmless in our particular case. The N2 method holds for a range of physical conditions broad enough to encompass both BCDs and QBCDs. Figure 16a shows the residual between the abundance determined with the N2 method, $[12 + \log(\text{O}/\text{H})]_{\text{N2}}$, and the T_e method, $[12 + \log(\text{O}/\text{H})]_{T_e}$,

$$\Delta[12 + \log(\text{O}/\text{H})] = [12 + \log(\text{O}/\text{H})]_{\text{N2}} - [12 + \log(\text{O}/\text{H})]_{T_e}, \quad (\text{A1})$$

for the set of ~ 310 metal-poor line-emission SDSS/DR3 galaxies analyzed by Izotov et al. (2006). The T_e based abundances are directly computed by the authors from state-of-the-art photoionization modeling, whereas the N2 abundances have been derived from the published line fluxes using the recipe in Pettini & Pagel (2004).

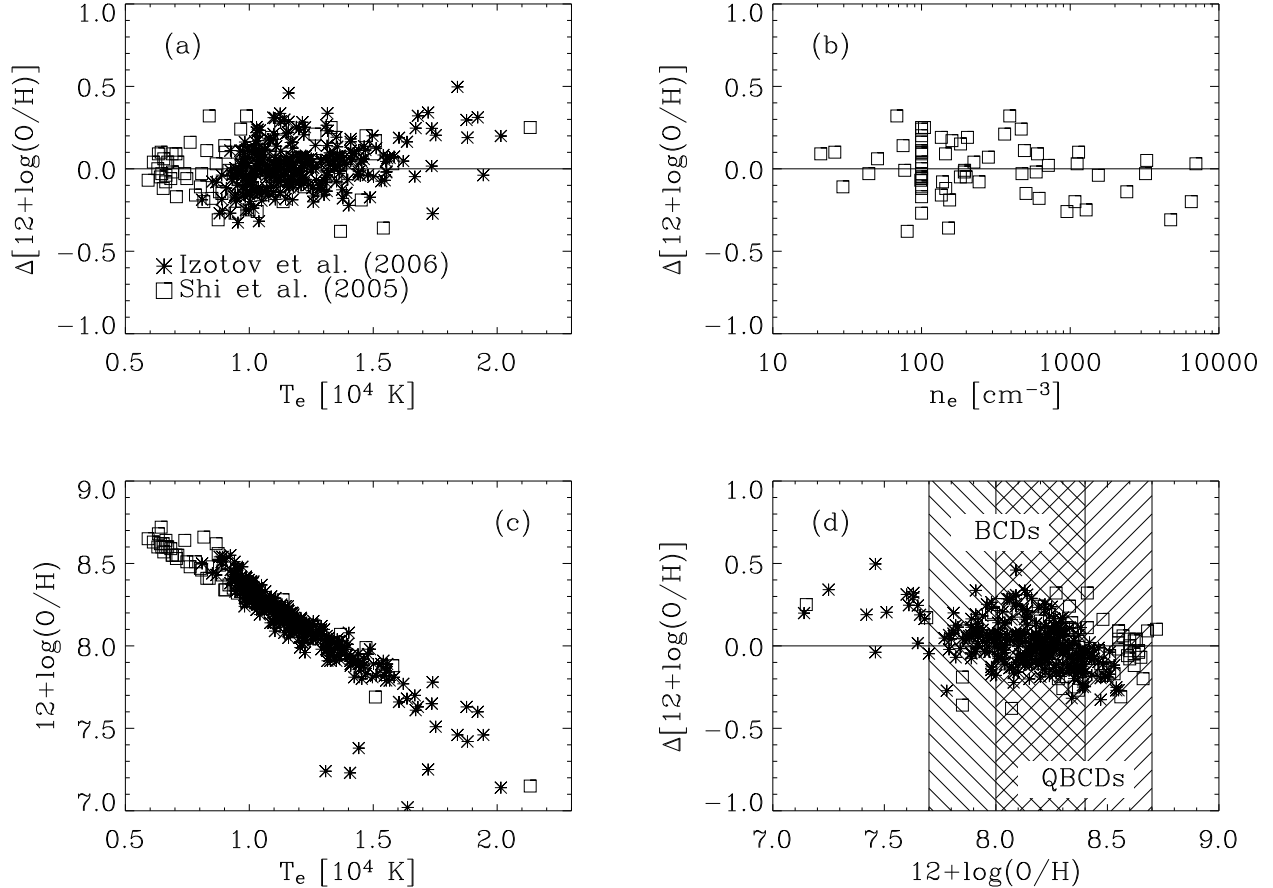


FIG. 16.— (a) Difference between the oxygen abundances determined with the N2 and the T_e methods, $\Delta[12 + \log(\text{O}/\text{H})]$, for the set of galaxies analyzed by Izotov et al. (2006, the asterisks) and Shi et al. (2005, the squares). They are represented vs the [OIII] electron temperature T_e . There is no systematic trend for $T_e \lesssim 17000$ K. (b) $\Delta[12 + \log(\text{O}/\text{H})]$ vs electron density n_e for the set of galaxies analyzed by Shi et al. (2005). No systematic trend. (c) Tight correlation between oxygen abundance and electron temperature for $12 + \log(\text{O}/\text{H}) \gtrsim 7.5$. (d) $\Delta[12 + \log(\text{O}/\text{H})]$ versus $12 + \log(\text{O}/\text{H})$. As indicated by the insets, the hashed regions correspond to the range of abundances of BCDs (the -45° slanted lines), and the QBCDs (the $+45^\circ$ slanted lines).

The difference is represented as a function of the [OIII] electron temperature. There is no obvious systematic difference between the two methods when $5000 \text{ K} \leq T_e \leq 17000 \text{ K}$. The hint at systematic deviation when $T_e \geq 17000 \text{ K}$ does not seem to affect our estimates (see below). Figure 16a also includes the difference computed by Shi et al. (2005)⁷ for a set of ~ 70 BCD galaxies (the squares), which we include because these authors also provide the second independent thermodynamic parameter, namely, the electron density n_e . Figure 16b shows the variation of the residual with n_e for Shi et al. (2005) galaxies, which evidences no systematic trend even though the large range of electron densities that are involved; $10 \text{ cm}^{-3} \leq n_e \leq 10^4 \text{ cm}^{-3}$. Finally, Fig. 16d shows the residuals vs the metallicity. Again residuals are independent of metallicity except at the low end when $12 + \log(\text{O}/\text{H}) \lesssim 7.5$. The strong-line methods work because the seemingly independent variables (T_e and n_e) are actually related to $12 + \log(\text{O}/\text{H})$ as a single parameter family (e.g., Stasińska 2004, § 2.1.2). This is the case for the dependence of T_e on $12 + \log(\text{O}/\text{H})$; see Fig. 16c. This tight correlation breaks down at $12 + \log(\text{O}/\text{H}) \lesssim 7.5$. Due to the correlation, the low abundance regime coincides with the high temperature points which seems to deviate from the nominal law as hinted in Fig. 16a. This potential problem at low abundances and high temperatures should not affect our sample of BCDs and QBCDs, whose abundances correspond to the well behaved part of the N2 calibration: see Fig. 16d, where the range of BCD and QBCD abundances are represented as hashed regions. Moreover, according to Figs. 16a and 16b, the range of T_e and n_e where the N2 calibrations hold covers the full the range of thermodynamic parameters to be expected in H II regions (e.g., Dyson & Franco 2000). These two facts indicate that the N2 abundance estimate is valid for both BCDs and QBCDs, even though their H II regions may have different physical conditions. Then the relative difference between the abundances of BCDs and QBCDs are not an artifact of using strong-line empirical methods. The *rms* variations of $\Delta[12 + \log(\text{O}/\text{H})]$ are 0.16 dex and 0.13 dex, for Shi et al. (2005) galaxies and Izotov et al. (2006) galaxies,

⁷ In this case the authors compute both the N2 and the T_e abundance estimates. They differ systematically by 0.2 dex, a constant term that we have removed when plotting since it does not affect relative differences between N2 abundances.

respectively. In the case of Izotov et al. (2006), we only consider $12 + \log(\text{O}/\text{H}) \geq 7.5$.